SLAC-PUB-3378
July 1984
A

# Surface Studies of Nb, its Compounds, and Coatings*

EDWARD L. GARWIN and ROBERT E. KIRBY
*Stanford Linear Accelerator Center*
*Stanford University, Stanford, California 94305*

Invited paper presented at the Second Workshop
on RF Superconductivity,
CERN, Geneva 23-27 July, 1984

* Work supported by the Department of Energy, contract DE-AC03-76SF00515

## 1. Introduction

The application of modern surface physics to materials of interest to this group was reviewed in meticulous detail at the 1980 Karlsruhe Workshop on RF Superconductivity by A. Septier. The presentation made here assumes familiarity with that work [Septier (1980)].

Common surface analytical techniques can be characterized in terms of the incident probe beam. Electron beams are used to determine atomic arrangement in low energy electron diffraction (LEED) and reflection high energy electron diffraction (RHEED). Topography is displayed with scanning high voltage electron microscopy (SEM), which instrument when fitted with an energy or wavelength dispersive x-ray detector becomes an electron probe microanalyzer (EPM) capable of determining near-surface chemical species and their lateral distributions. Electron beams incident at a few kV allow Auger electron spectroscopy (AES) of the emitted lines specific to the elements bombarded and with occasional rough information about chemical valency of bound atoms. Electron bombardment coupled with a mass spectrometer allows electron impact desorption (EID) to provide information on the nature and threshold of desorbed species. A rather unusual use of an electron spectroscopy has been use of Josephson junction tunneling to investigate the quality of surface treatment as it affects superconducting Nb [Gurvitch and Kwo (1984)].

Using photons as the incident probe, ellipsometry (ELIP) in the optical region measures the complex index of refraction, which under ideal conditions of surface flatness and known compound formation can follow film growth from fractional monolayers and, uniquely, can do so for pressures ranging from UHV to above atmospheric. For incident photons of energy from the vacuum ultraviolet through the soft x-ray region, photo-electron spectroscopy for chemical analysis (ESCA), designated UPS or XPS for incident ultraviolet light or x-rays respectively, identifies near-surface atoms, can give detailed information of their valence states. With variable take-off angle, XPS can non-destructively give information on depth distribution of layered structures. ESCA with a synchrotron

light source tunable in energy becomes an exquisite tool with a variable depth of analysis. X-rays are also used in glancing angle x-ray diffraction to positively identify the composition of some grown films [Wittmer et al (1981)].

With incident ions, low energy ion elastic scattering (LEIS) gives information on the presence at the outermost surface layer of specific masses, and has been used to determine adsorbed molecular orientation (CO on Ni and W). The higher energy Rutherford backscattering (RBS) can both identify masses and give extended depth distribution data non-destructively. Ion sputtering of surface species is used both to surface profile (peel the onion), allowing other spectroscopies to destructively analyze in depth, and also with secondary ion mass spectrometry (SIMS) to determine surface species with extreme sensitivity for the alkali metals and hydrogen (Group IA), and good sensitivity for Group IIA plus boron and aluminum. SIMS is the only direct method for observing hydrogen, and with quadrupole mass analyzers capable of $m/e \geq 500$, is also useful to study sputtering of clusters, as an aid to determining surface composition. Both SIMS and ion-sputter profiling can lead to formation of surfaces or near-surface layers of stongly altered compositions due to preferential sputtering and diffusion mechanisms. Such effects have been explored for $Nb_3Sn$ [Smathers (1980)], for the oxides of Nb [Karulkar (1981)], have been discussed in a short article [Wehner (1982)], and have been the subject of an extended literature survey of over 60 references [Betz (1983)] which produced a table of experimental results of preferential sputtering on many alloys and compounds.

This review is strongly rooted in experiment. Those who long for extensive theoretical discussions seek here in vain. I have, however, attempted to give an extensive bibliography in areas which are relatively unknown, such as thermal-field emission, or sputtering of multi-component materials. The scope of this review was strongly limited by available time; absence of any particular area of work or publication is not at all a judgment on its quality.

## 2. The Nb-Vacuum Interface

Presence of a dielectric layer at the vacuum interface has long been known to enhance secondary emission and multipacting. The presence of interface oxides of the general structure $NbO_x$ was postulated [Halbritter (1981)] to cause rf losses, to enhance electron tunneling into the vacuum, and to weaken the superconducting interaction at the Nb-$Nb_2O_5$-interface [Halbritter (1982)]. Details of the niobium-vacuum interface obtained by XPS, LEIS, and AES were previously described [Septier (1980)]. He included studies on oxide growth and oxide coatings on niobium carried out with the aid of argon sputter profiling and XPS deconvolution techniques [Grundner (1980 A)], whose detailed quantitative picture of the Nb-oxide interface is called in question by subsequent studies on the effect of sputtering on the surface composition of samples of NbO, $NbO_2$ and $Nb_2O_5$ which concluded [Karulkar (1981)]:

> "We found it very difficult to use the sputter depth profiling technique to obtain information about the composition and structure of thin niobium oxide films. ***Apparently,*** one observes all the intermediate oxide compositions while sputtering from the surface pentoxide to the metallic Nb beneath it. Unfortunately, most of the drastic composition changes are brought by the inert ion beam itself..."

The qualitative picture of the Nb-oxide interface proposed [Grundner (1980 A)], is supported by synchrotron light beam UPS on Nb and $Nb_3Sn$ [Miller (1982)] who found for Nb:

> "We may summarize our findings for the oxides as follows: We find three stages of oxide formation when the clean Nb surface is exposed to oxygen. Of the three oxide stages the final saturation oxide has a chemical shift characteristic of the "air oxide" surface, generally accepted to be $Nb_2O_5$. The suboxides appear to neither grow homogenously across the surface nor grow an abrupt oxide-metal interface into the bulk."

Considerable research has subsequently explored techniques of protecting Nb surfaces by cleaning treatments and subsequent growth or application of protective layers. Several approaches will be reviewed here. In recent years new choices of cavity geometries which inhibit multipacting have been successfully applied to the construction of superconducting accelerator structures. The problem re-

mains, however, of decreasing or eliminating the effects of multipacting in parts of the structures for which the geometry cannot be significantly changed, such as in higher-order-mode couplers. In these cases the suppression of multipacting can be achieved by coating the surfaces of interest with a material which must have both a low secondary electron emission (SEE) coefficient and low RF losses, and which also protects the Nb against oxidation in order to maintain the original high unloaded Q and accelerating field of the cavity. Materials such as NbC, NbN, TiC and TiN seem to be good candidates for this purpose. They are good electrical conductors and possess rather high superconducting transition temperatures [Toth (1971)].

## 2.1 Coating Research at SLAC

TiN is routinely used at SLAC as a proven anti-multipacting coating for inter-cavity coupling slots, RF windows and RF coupling loops on non-superconducting surfaces. Preliminary surface physics studies on this material indicated that the as-deposited films exhibited low SEE yields, but exposure to air caused the SEE yields to increase so much that such films would appear useless as anti-multipacting coatings. To explore the apparent contradiction between experiment and practice, those conditions were examined which might lead to an in-situ lowering of the SEE yield. One such condition is electron-bombardment of the TiN-coated surfaces during initial running of RF devices.

Apparatus The experimental apparatus consisted of a stainless steel UHV analysis chamber linked to a process system chamber via magnetically coupled sample transfer mechanism (Figure 1). The presssure was typically $2x10^{-10}$ Torr in the analysis chamber and $1x10^{-9}$ Torr in the process chamber.

A Vacuum Generators CLAM 100 XPS unit controlled by an LSI-11 computer was used to collect AES and XPS data using electron counting techniques. The secondary electron emission (SEE) yield data were collected using an electron beam at normal incidence, a programmable high voltage power supply and an electrometer which were also under computer control (Figure 2).

The samples were single crystal Nb discs of unknown orientation, 1.6 cm

diameter x .5 cm thick cut from 2500$^o$ K-outgassed low-Ta rods, mechanically polished with .5$\mu$m diamond paste and electropolished in 10% HF - 90%$H_2SO_4$ solution which removed approximately 50$\mu$m of Nb surface.

The discs were sputter-cleaned and the various films were sputter-ion deposited using a Kaufman-type [Reader et al (1975)] ion source. The films were deposited to a thickness of 140Å as determined by using a quartz-crystal thickness monitor, this being the thickness of the TiN coatings previously used successfully at SLAC. Immediately after deposition the samples were transferred to the analysis tank for the SEE, AES, and XPS measurements.

The SEE measurements used a retarding voltage method in which a 1.5 KeV electron beam with a current of 2 nA strikes the sample whose potential is varied from -50 to -1450 volts in 10 volt steps. The current flowing through the sample was measured at each retarding voltage by an electrometer, and the total secondary yield $\sigma$ was calculated using: $\sigma$= 1 -(target current/primary current).

The AES measurements used an electron current of 50 nA rastered over approximately .25 cm$^2$ of the sample. The analyzer was operated in the constant retard ratio (CRR, energy resolution $\sim$ 1%) mode for the AES measurements.

The XPS data was collected using a Mg anode bombarded with 12 KeV electrons at 20 mA. The VG analyzer was operated in the constant analyzer energy (CAE, energy resolution $\sim$0.75 eV) mode with a pass energy of 20 eV. Photoelectrons were collected from a .17 cm$^2$ sample area, chosen to fall within the area dosed in the electron beam exposure experiments to be described later.

After the data on the as-deposited films was collected, the samples were moved to a loading chamber where they were exposed to room air (22$^o$C, 50% RH) at atmospheric pressure for one hour. The loading chamber was then evacuated and the samples were transfered back to the analysis tank for characterization as described above.

The electron beam exposures were at an energy of 1067 eV and a current of 400 nA rastered over .98 cm$^2$ for the 140Å TiN and NbC and 80 nA rastered over .37 cm$^2$ for the 15Å TiN, 140Å NbN, 140Å TiC films and the oxidized uncoated

Nb surface.

When referring to the accompanying diagrams, (a) refers to the as-deposited films; (b) refers to the films exposed to air; and (c) refers to the results after electron beam bombardment. Data is also presented for the clean Nb substrate and its air oxidized surface. The plots are offset vertically with respect to each other for clarity.

The SEE measurements indicate that the lowest $\sigma$ occurs on the as-deposited films. In some cases $\sigma$ remains less than unity over the entire incident energy range 50-1450 eV. After exposure to air $\sigma$ rises substantially. Subsequent electron beam bombardment serves to reduce $\sigma$, in some cases to nearly the value obtained for the as-deposited film.

The AES measurements of the as-deposited films show the elemental compositions of the surfaces of the films. In addition to the primary elements of the deposited materials small amounts of oxygen are seen on some of the layers. This is probably due to $H_2O$ desorption from the chamber walls during sputter deposition. After exposure to air an increase in the oxygen peak area is noted along with a small increase in the carbon level. Changes in the structure of the primary AES peaks will reflect changes in the chemical composition of surface layers in our data. After electron beam bombardment, only small changes in the AES spectra are seen, compared to the oxidized overlayers, indicating that the relative amounts of each element are largely unaffected. Retrieving information about chemical states is difficult due to the nature of the AES technique and quantitative analysis of these spectra was therefore not undertaken.

The XPS data gives more easily extractable information about the chemical states present in the films but probes to a greater depth than AES. After deposition, XPS shows primarily the material sputtered onto the Nb discs with some films incorporating small amounts of oxides (again, due to $H_2O$ desorbed from the chamber walls during sputter deposition). After exposure to air the amount of oxide present in each material rises significantly with a concomitant decrease in the primary species, and a shoulder in the XPS O1*s* peak consistent

with water adsorption. After electron beam bombardment XPS shows that the oxide levels are slightly reduced by the bombardment, while the $H_2O$ shoulder is reduced significantly more.

In addition to XPS, AES and SEE, we have made some electron-induced--desorption (EID) measurements of the oxidized layers on Nb and NbN/Nb. $O^+$ emission is observed whose desorption rate increases with e-beam exposure, in agreement with the observations of others [Lin et al (1979)]. This rate increase is due to a rise in the surface concentration of weakly bound surface oxygen, created during reduction of the $Nb_2O_5$ to sub-oxides by electron bombardment.

2.1.1 RESULTS

The results of the measurements described above are given in Figures 3-20. In these figures, there is a consistent convention:

(a) As cleaned or deposited

(b) oxidized at 1 atm, 3600 sec.

(c) electron bombarded (dose rate and total dose indicated)

Clean Nb The results presented here for clean sputtered Nb are similar to those which we have obtained for furnace-cleaned Nb (2300K, 21 hrs. at 3 x $10^{-10}$ Torr). Sputtered surfaces can always be made C and O-free whereas we have observed very small amounts ($<5\%$ of a monolayer) of O on all furnace-cleaned samples. This appears to be due to dissolved O from the bulk diffusing to the surface during heating. For both types of cleaning, however, we obtained essentially identical XPS, AES and SEE data.

Transition Metal Carbide and Nitride Overlayers Using these materials as secondary electron suppressors on Nb would seem to be an ideal choice. They are excellent electrical conductors, have low secondary emission coefficients and high superconducting transition temperatures [Toth (1971)]. From the data, we see that $\sigma$ is quite low for these as-deposited overlayers on Nb and that the electron backscatter contribution at higher primary energy is smaller than that for uncoated Nb (compare for example, $\sigma$ for clean Nb and 140Å TiN/Nb). At this

time, the mechanism for reduced secondary emission in transition metal carbides and nitrides is not understood.

Oxidized Nb and oxidized Overlayers Upon exposure to air (and pure oxygen, as well, we have found), the bare Nb surface and its overlayers form thin surface oxides at the exposures used in this experiment. For instance, clean Nb oxidizes to about 10Å (4) and we expect that the overlayers oxidize to a similar depth, for example, the 15Å TiN overlayer does not quite fully oxidize, (i.e., significant TiN concentrations are present in the Ti core level spectra) according to the XPS results. XPS shows the presence of $Nb_2O_5$ (as well as sub-oxides) for oxidized Nb, NbN and NbC. $TiO_2$ is observed for TiN and TiC oxidized overlayers. AES (which probes a shallower depth) confirms these observations.

The oxidation results for TiN are surprising in the light of investigations of the oxidation kinetics of 2300 and 3200Å TiN films made by RBS [Wittmer (1981)]. They oxidized TiN in a furnace flushed with dry $O_2$ at temperatures of 500°C to 650°C, and found the oxide thickness, d, to be diffusion limited

$$d = 2(Dt)^{1/2} \tag{1}$$

where D is the coefficient of oxygen diffusion in $TiO_2$, and t is the oxidation time. They calculated D from an Arrhenius plot (log D vs 1/T) to be:

$$D(T) = D_0 exp(-E_a/kT) \tag{2}$$

where k is Boltzman's constant, T is the temperature, $E_a = 2.05$ eV is the activation energy, and the pre-exponential factor $D_0 = 4.3 \times 10^{-2}$ $cm^2/sec$. Calculating the oxidation thickness of TiN from Eq (1) at 300°K gives $d = 1.5 \times 10^{-8}$ Å! It remains for us to determine whether the TiN films were columnar or discontinuous, other processes operate in moist air, or processes attendant to electron and/or photon bombardment during measurement promoted oxidation and diffusion of oxygen through them, as has been observed for C under electron bombardment[Garwin (1981)].

The SEE yield shows a large increase upon oxidation, a result which is expected for bulk oxides and observed here for very thin oxides and which may be

due to the $H_2O$ resonant tunneling mechanism [Halbritter (1984 B)] or to charging. Surface charging of $<$1eV has been observed in thin MgO layers [Gibson et al (1982)] and oxidized Nb [Grunder et al (1980 B)], so it is reasonable to believe that charged holes can be generated in the oxidized layer through pair production. The presence of this positively charged layer results in a drop of the work function [Bronshtein et al (1965)] and the presence of an accelerating field across the oxide [Grundner et al (1980 A)], either of which results in increased secondary electron emission thereby accounting for the observed increase in $\sigma$ upon oxidation.

Electron-bombardment Continued electron-bombardment of the oxidized overlayers produces damage in the form of broken bonds, reduced oxides, excited species, mobile and immobile holes, etc. This is reflected in $O^+$ being electron-desorbed as described in the EID results above. The desorbing $O^+$ (and possibly neutral CO and $CO_2$) is also observed as a small change in the XPS O signal and AES C and O signals. The SEE yield, however, shows a large change in value as a result of this bombardment. Electron-bombardment generated damage in the oxide results in a good conducting layer (i.e. the oxide turns metal-like), and the surface charge, which sustained the increased SEE yield observed before bombardment, vanishes; $\sigma$ drops back toward its value for the unoxidized surface. In fact, visible discoloration of such a bombarded area has been observed by others [Lin et al (1979)], as has the appearance of free metal in the oxide layer with larger electron exposures than those used here. The decrease in $\delta$ definitely can not be ascribed to buildup of polymerized hydrocarbon or carbon layers in this case, as has been previously suggested [Grundner (1980 B)].

Cavity Tests of TiN Films at SLAC The S-band cavity used in the studies of the microwave properties of coatings of TiN was a doubly-reentrant type having the highest electric field between the posts to encourage multipacting. The cavity was tested before and after coating of both posts with 150Å of TiN by sputtering. In contrast to the negative experience of the Cornell Group [Padamsee (1977)] with TiN-coated muffin-tin cavities, the SLAC group [Campisi (1983)] found:

"The first set of measurements performed on the RF multipacting properties of an S-band doubly-reentrant niobium cavity has shown that multipacting is entirely suppressed when TiN films are deposited on selected regions of the surface. The cavity multipactors very easily without the coating. The films do not show any appreciable dielectric losses. The unloaded Q was the same for the uncoated cavity and when only the end surfaces of the posts were coated [$Q_0 = 2.5 \times 10^7$ (4.2K) and $7 \times 10^7$ (1.35K)]. Some current losses were observed when also part of the lateral surface of the posts was coated [$Q_0 = 2.1 \times 10^7$ (4.2K) and $4.2 \times 10^7$ (1.34K)]. These additional losses should not compromise the operation of superconducting Nb cavities at 4.2K when coated with TiN films."

## 2.2 Nb Interfaces Investigated with Josephson Junctions

The first application of the oxidized metal overlayer (OMO) technique in tunneling used an 80Å overlayer of Al on $V_3Si$ with a Pb counterelectrode [Hauser (1966)]. Earlier OMO work is reviewed, and their recent extensive OMO work is summarized by Bell Labs scientists M. Gurvitch and J. Kwo in an article which contains an extensive bibliography [Gurvitch (1984)] to which interested readers are directed. The work reported below is that of Gurvitch and Kwo and represents results from Nb films deposited by magnetron sputtering onto smooth, oxidized silicon substrates. Appropriate cautions apply to direct extension of their results to surfaces of Nb cavities which may be much rougher. The characteristics of broad area Nb/Al oxide-$Pb_{0.90}Bi_{0.10}$ junctions are shown in Fig. G4 for different thicknesses of aluminum deposited on the Nb film and oxidized in air for 20 minutes (the d=0 native oxide junction was formed by air oxidation of the Nb for 4 days.) As an aid in interpreting these curves, Fig. G6 shows schematically the density of states (DOS) a tunneling structure with a clean superconducting gap in the Pb-Bi, and a tail in the DOS in the Nb. The detailed interpretation of the figures is complicated, but put simply, an ideal proximity layer will not produce any sub-gap leakage. From Fig. G4 it is seen that for Al thickness $\geq$100Å no sub-gap current is seen at or below $\Delta_{PbBi}$. It therefore appears that while even thin Al layers reduce oxygen contamination, the thicker layers prevent it completely.

The oxide tunneling resistance is shown in Fig. G10 as a function of deposited

metal layer thickness, $d_m$ for various metals at 77°K. The estimated resistance at $d_m = 0$ is $10^{-7}\Omega cm^2$. The very large changes in resistance with $d_m < 10$Å indicates that such layers must already be essentially continuous and pinhole-free on these smooth substrates. Fig. G10 also shows that the order of increasing oxidation rate for the overlayer metal is Al, Mg, Er, Y.

Many all-refractory junctions (both electrodes Nb) were prepared and extensively evaluated. A population of 400 junctions was cycled between 300°K and 6°K 4880 times with no failures due to shorts and no change in average initial currents. Fig. G11 shows the results for the average critical current of these junctions after annealing. At temperatures between 150°C and 250°C, the current decreases and saturates with time, and it is speculated that this is due to dissociation of aluminum hydrides in the oxide with the released oxygen combining with excess metallic Al (or Nb) to form oxides which increase the barrier width or height. The dispersion in critical current the the junction quality remained unchanged during these anneals. At temperatures of 275°C and higher the current no longer saturated within a few hours, suggesting continuous diffusion of oxygen to the barrier. Severe oxidation of the contact pads prevented extended measurements. Junctions of the above type have been stored in room temperature air since 1981 without change in their nearly ideal junction characteristics.

Surface oxidation studies of the Nb/Al overlayer structures were made by XPS, in order to shed light on puzzling shape of the Al junction resistance curve of Fig. G10, and of the fact that proximity effects of excess unoxidized Al was not observed for $d_{Al}$ <100Å. Nb/M layers were prepared, oxidized in air for 15-30 min., and pumped overnight without bakeout before XPS spectra were taken, at a pressure of $\sim 10^{-8}$ Torr. The overlayer thicknesses are given in Table I, while the XPS data are displayed in Figs. G12 and G13 for $Nb^{3d}$ and $Al^{2p}$ regions, respectively. Fig. G12a shows the usual Nb, $Nb_2O_5$, and $NbO_x$ suboxide structure for air-oxidized Nb, while Fig. G12b shows the surprising result that Nb oxidation is completely suppressed by the 38Å Al overlayer. Nb oxide is detected for dAl < 9.5Å under these oxidation conditions, and after "prolonged oxidation" for thicker Al overlayers. It is found that (starting at the vacuum)

the layer configuration is $C/Al_2O_3/Al/Nb$. By varying the take-off angle and assuming plane parallel layers, quantitative analysis gave the results in Table I, which show that for deposited layers thicker than 10Å, the thickness of the oxide layer and of the residual metal layer does not account for all the metal deposited. The puzzling results mentioned earlier, and the vanishing metal of the overlayer were consistently explained by a mechanism in which the excess metal of the overlayer diffused into the grain boundaries of the Nb, as indicated in Table I for Al and Mg. Further experiment showed that such diffusion did not take place on samples prepared at room temperature, but did occur at temperatures of $\sim 150^{o}C$, as is evident from recent XPS and (unpublished) Auger studies.

**Table I. Thicknesses of OMO's**

| Nb/Al overlayer Sample No. | Thickness of deposited Al overlayer (Å) | Thickness of $Al_2O_3$ (Å) | Thickness of residual metallic Al (Å) | Thickness of metallic Al lost by diffusion (Å) |
|---|---|---|---|---|
| I. | 9.5 | 12.3 | 0 | 0 |
| II. | 38.5 | 20.4 | 2.0 | 21 |
| III. | 112 | 9.1 | 9.2 | 96 |
| **Nb/Mg overlayer Sample No.** | **Thickness of deposited Mg overlayer (Å)** | **Thickness of MgO (Å)** | **Thickness of residual metallic Mg (Å)** | **Thickness of metallic Mg lost by diffusion (Å)** |
| I. | 10 | 7.6 | 0 | 0 |
| II. | 16.6 | 7.9 | 1Å | 7 |
| III. | 45 | 7.0 | 4.9 | 32 |
| IV. | 65 | 12.5 | 6.1 | 43 |

Nb/Y overlayer structures were studied over the range of 4.3Å to 30Å of Y, whose oxygen affinity was so strong that such overlayers not only protect Nb against oxidation, but actually reduce submonolayer amounts of NbO at the Nb/Y interface. Fig. G14 gives $Nb^{3d}$ XPS spectra for Nb cleaned in vacuum and with a 112Å overlayer of Al. The data for Nb/Y are essentially identical with the cleanest Nb results of the figure.

Alloy formation and oxidation of a Nb-rich Nb-Al alloy has been studied by the group of W. Spicer using core level photoemission in combination with synchrotron light [Oshima (1983)]. Exactly the same chemical shifts were observed from both the $Nb_xAl$ alloy (with x = 4- -5) and from a Nb surface onto which Al had been evaporated, indicating similar structural arrangements. The oxidation rate of Nb in these structures was about 100 times less than for pure Nb or $Nb_3Sn$ for $O_2$ exposures of 30L. Above 300L, $Nb_2O_5$ forms rapidly as the oxidation barrier of the top aluminum layer is broken. Two stages in the oxidation process of the Nb-Al alloy were identified; 1) Al-O and Nb-O formation at a few x 10L, and 2) $Al_2O_3$ and $Nb_2O5$ formation above 100L. The stages were distinguished clearly in terms of Al2p, Nb4p, and O2p chemical shifts.

### 2.3 Extension of OMO Results to Cavity-like Surfaces

The surface physics group at SLAC has applied Gurvitch and Kwo's results by evaporating 17 and 25Å layers of Al onto sputter-cleaned bulk Nb, and subsequently exposing the structures to air for $\sim$1 hr., with the result that barely discernible oxidation of the underlying Nb was seen, while oxidation of the Al was almost complete. Because the evaporation process is line-of-sight, Al may not have completely covered the rough sputtered surface. The experiment will be repeated with a sputtered deposit to improve the "throwing power". The next step is to seal the Al (or Y) with a thin continuous metal film (such as Pt or Rh) which will prevent oxidation on air exposure as will occur in accelerators even if only by accident. It seems imperative to prevent oxidation of the active metal layer for the following reasons: 1) As demonstrated earlier in this paper, oxides increase the secondary emission yield. 2) Surface charging of oxides can lead to large field electron emission currents, expecially in hydrated oxides. 3) Oxides will eventually penetrate extended reactive metal overlayers on cavity surfaces and allow their oxidation, in contrast to the geometry of junctions where diffusion into the active area must take place through the extended edge of the reactive metal layer. 4) Because most oxides have very low thermal conductivity, thick aggregates can enhance field emission by thermal effects, according to the unified theory of temperature-field (T-F) emission developed by [Christov (1966–1978)],

amd evaluated by Bermond et al [Bermond (1974)].

As an aside, Christov's work seems to have been unnoticed in the rf superconductivity field, although Klein and Turneaure [Klein (1983)] have referred to a CERN report on "thermal field emission" [Rohrbach (1971)] from which they derive Fig. KT6, field emisison as a function of emitter field and temperature for a metal. In case that work is not reported here, they state:

> "Since field emission in cavities is usually observed only in restricted field intervals one will normally not notice the curvature of the field emission characteristic of a hot emitter.....The slope will yield a $\beta'$ which is higher than the actual enhancement factor ($\beta = 200$) and which furthermore depends on the location of the viewed field interval on the E-axis (see Fig. KT6). ...Thus the anomolous behavior of $\beta$ is traced back to the use of the wrong theory ($T = O^oK$) for the analysis of experimental data ($T >> O^oK$)."
> And they further conclude:
> "It has been shown with a specially designed superconducting resonator that rf field emission exhibits identical features as broad area dc field emission. The rf field emission data can also be interpreted in the framework of the Fowler-Nordheim theory if a microscopic field enhancement factor $\beta \simeq$50-200 is assumed at the emitter..."

## 2.4 Use of Active Metal Layers to Purify Bulk Nb

Encouraged by the results of Gurvitch and Kwo showing the deoxidizing effect of Y on Nb, the group at Cornell has evaporated Y on Nb held at 1250$^o$C for a few hours to purify bulk Nb and so have significantly raised the RRR of elliptical cavity half-shells prior to welding with salutary results on the maximum field gradient [Padamsee (1984)]. In addition, F. Palmer and M. Tigner of the Cornell group have begun experiments to determine the effects of the Nb oxide layer on the microwave resistance of superconducting Nb, by measuring $R_s$ on Nb whose oxide layer has been diffused into the bulk, and then remeasuring $R_s$ after controlled surface oxidation processes. Their results will be presented at this conference and may produce the first definitve experimental information on the effects of surface oxides on rf superconductivity and field emission, when combined with the results of synchrotron light studies [Oshima (1983)]. Suitable procedures should be used to avoid enhancing oxygen reactivity by the presence of hot filaments, as has been seen with GaAs [Pianetta (1978)].

## 2.5 Gas Discharge Treatments on Electron Emission of Nb

An extensive and interesting study has been made of the interrelated effects of baking (300°C for 24 hr) and of gas discharge in pure argon, argon with 10% oxygen, methane, and nitrogen [Dominichini (1984)]. Effects of these treatments on field emission and on secondary emission were determined in a UHV system in the larger context of emission effects produced by subsequent exposures as might occur in accelerator operation, and of further in-situ treatments to restore desirable surface properties.

Dominichini and Hilleret's results of surface treatment as they effect surface emission are summarized in Table II. After bakeout, field emission from the sample is not reproducible. With careful application of voltage to avoid breakdown, the surface conditions, and allows determination of the applied field for an emitted current of $10^{-8}$, and of corresponding values for $\beta$, the field enhancement factor. The measured field valve varies by a factor of 2. Following gas discharge in pure Ar (to a dose of 3 x $10^{18}$ ions/cm$^2$), the I-V characteristics become very stable ($\pm 10\%$), but the field for $10^{-8}$A is lower than the valve obtained after conditioning of the baked-only surface. If the Ar discharged surface is now bombarded again for the same dose in Ar + 10% $O_2$, the current drops by 3 orders of magnitude at comparable field values, as seen in Table II. If the breakdown threshold is exceeded, however, violent discharges occur and the benefit of this treatment is found to be entirely lost, and electron microscope pictures of the damaged area shows numbers of asperities.

Similar measurements have been carried out on the effects of treatment on secondary emission coefficient, $\delta$. A generalized yield curve is given in Fig. DH11, which defines some of the terms used to summarize their results in Table III.

## TABLE II

| Measurement (at 0.4mm, except * at 0.2mm) | Field (MV/m) (for $10^{-8}$A, except † for $10^{-11}$A) | $\beta$ |
|---|---|---|
| BAKED SAMPLE | | |
| MA13 | 12 | 233 |
| MA14 | 15.5 | 115 |
| MA18 | 31.5 | 68 |
| MA19 | 39 | 63 |
| AND ARGON DISCHARGE | | |
| MA29 | 19.2 | 159 |
| MA30 | 20 | 143 |
| MA31 | 20.5 | 159 |
| MA32 | 21 | 148 |
| MA33 | 21 | 165 |
| MA34 | 21 | 160 |
| AND ARGON + 10% $O_2$ DISCHARGE | | |
| MA41 | 18† | |
| MA56 | 43† | |
| MA63 | 20† | |
| MA64 | 44† | |
| MA77* | 36† | |
| MA78* | 78† | |

## TABLE III

| TREATMENT | $\delta_{100eV}$ | $\delta_{1000eV}$ (eV) | $E_1$ (eV) | $E_2$ (eV) | $E_{max}$ | $\delta_{max}$ |
|---|---|---|---|---|---|---|
| AS RECEIVED | 2.47 | 1.8 | - | - | 250 | 2.79 |
| BAKED (300°C, 24h.) | 1.2 | 1.17 | 60 | 1550 | 300 | 1.48 |
| GAS DISCHARGE IN NITROGEN | | | | | | |
| After Discharge | 0.83 | .94 | 150 | 750 | 400 | 1.09 |
| 94 h. $N_2$ | 1.01 | 1.03 | 100 | 1100 | 400 | 1.23 |
| rebaked | 0.9 | .99 | 150 | 950 | 300 | 1.23 |
| 48 h. air | 1.07 | 1.13 | 70 | 1450 | 350 | 1.42 |
| rebaked | 1.07 | 1.09 | 90 | 1300 | 300 | 1.37 |
| GAS DISCHARGE IN ARGON | | | | | | |
| After discharge | 0.87 | .98 | 115 | 980 | 300 | 1.25 |
| 8 h. air | 1.5 | 1.4 | 38 | - | 300 | 1.86 |
| rebaked | 1.03 | 1.05 | 90 | 1150 | 300 | 1.31 |
| GAS DISCHARGE IN METHANE | | | | | | |
| After discharge | 1.75 | .9 | 140 | 850 | 200 | 2 |
| GAS DISCHARGE IN ARGON + 10% $O_2$ | | | | | | |
| After discharge | 1.03 | .94 | 120 | 1100 | 350 | 1.25 |
| 66 h. $N_2$ | .99 | 1.08 | 103 | 1250 | 350 | 1.32 |
| rebaked | .96 | 1.07 | 105 | 1250 | 350 | 1.31 |
| 66 h. air | 1.09 | 1.16 | 80 | 1570 | 350 | 1.44 |
| rebaked | 1 | 1.1 | 100 | 1350 | 350 | 1.35 |

In Table III, $\delta_{100eV}$ and $\delta_{1000eV}$ are the values of $\delta$ for 100eV and 1000eV incident electrons, respectively. The detailed shapes of yield curves taken after various surface treatments is given in Fig. DH12. Their recommendations follow from inspection of Table III.

a) If it is technically possible to effect a gas discharge in situ, or to maintain the piece in nitrogen, a gas discharge in nitrogen is indicated.

b) If an air exposure is required and it is not possible to rebake, gas discharge in nitrogen or argon gives the best result.

c) If the piece may be rebaked after air exposure, a discharge in pure argon is recommended.

Dominichini and Hilleret's work is quite extensive, and contains much information, including Auger analyses which are beyond the scope of this short summary. It is to be hoped that the work will be published soon.

## 3. Surface Physics Studies of $Nb_3Sn$

### 3.1 Synchrotron Light Studies on $Nb_3Sn$ Formed In Situ

The oxidation properties of surfaces of Nb and $Nb_3Sn$ (the latter formed in vaccum by evaporation of Sn onto Nb) were studied at room temperature by the group of W. Spicer using photoemission spectroscopy with synchrotron light [Miller (1982 A and B)]. They find [Miller (1982 B)] that $Nb_2O_5$ is formed on oxidation of both Nb and $Nb_3Sn$. However the oxides of the Nb surface extend to a greater depth than for $Nb_3Sn$, and AES confirms the growth of oxides saturates at a lower exposure for $Nb_3Sn$ than for Nb.

They conclude:

"In summary, we can use the photoemission and Auger electron spectroscopy results to propose a model for the room temperature oxidation of $Nb_3Sn$ where a thin oxide (10-15Å) consisting of $SnO_2$ and $Nb_2O_5$ is formed as a protective layer. This is in contrast to the Nb metal oxides whre the NbO, $NbO_2$ and other suboxides grow deeper into the bulk (>20Å). The tin oxide, $SnO_2$, thus may have an important effect on the diffusion of oxygen through the surface oxide layer."

The studies described above were carried out on clean $Nb_3Sn$ surfaces formed in situ and held in $10^{-10}$ Torr vacuum.

### 3.2 Field- and Secondary- Emission of Furnace-Diffused $Nb_3Sn$

In a more technologically oriented experiment [Arnolds-Mayer (1982)], samples of $Nb_3Sn$ from 0.5 to 2 $\mu$m thick were formed by vapor diffusion of tin onto niobium sheet material in a specially constructed oven at the University of Wuppertal, simultaneously with the preparation of 8GHz cavities. The samples were then taken to CERN and examined in a UHV system with facilities for AES, total secondary yield measurement, and field emission measurement. In order to avoid surface modification due to electron bombardment, the secondary yield was measured with short pulses, each applying only $\sim$5 x $10^8$ $e^-$ on a 1 $mm^2$ area. Some samples were oxidized by anodization, and once in the system could be cleaned by Ar glow discharge (AGD). Auger spectra of an anodized sample is shown in Fig. A-M3, a) as received, b) after 1 min AGD, and c) after what the authors say is "complete removal" of the oxide layer, although apparently a clear oxygen signal remains, while the carbon has been converted to a carbide form. The AES data also clearly show the non-stochiometry (Nb-rich) of the sputtered surface, due to the high preferential sputtering of Sn [Smathers(1980)]. The secondary yield curves are shown in Fig. A-M4 for different oxide layer thicknesses a) as received, and b) after 1 minute AGD. It is clear that for these dirty surfaces, as received, anodization has reduced the secondary yield and after AGD the anodized layers produce $\delta$ curves with a lower first crossover ($E_{p_1}$)and a lower second crossover ($E_{p_2}$) than for non-anodized surfaces. The latter is not surprising because of the reduction in Z (and therefore backscattering) due to incorporation of oxygen. The secondary yields for unanodized $Nb_3Sn$ as received, after bakeout, and after

AGD are given in Fig. A-M5. Unfortunately concomitant AES spectra which would shed light on the effects of Sn diffusion on the surface composition are not presented. It is clear that AGD is necessary to produce acceptably low values of $\delta$. Measurements of field emission will presumably be reviewed by Latham, but did show that anodic oxide layers reduced field-emission. After AGD, the currents at a fixed field were in inverse proportion to the oxide thickness, and were decreased by a factor $\sim$ 100. On unanodized samples the same current reduction was found after bakeout, while AGD on these baked samples increased emitted currents. In all cases, sparking led to large enhancements of emitted currents.

### 3.3 SIMS, XPS AND AES ON FURNACE DIFFUSED $Nb_3Sn$

Another evaluation of samples produced at the University of Wuppertal in a larger furnace was undertaken at SLAC. The analysis system described in Section 2.1 has a SIMS capability with a micro focus ion gun operated at 1500 V, low fluence ($0.1\mu A/cm^2$) and a quadrupole operated at 500 AMU range. Macro ion bombardment removal is with a 13mm-dia homogeneous ion beam run at 1500eV and $7.5mA/cm^2$. The as-received sample was found to be moderately contaminated (1/2 to 1 monolayer) with carbon (AES), Fig. K2. Surface Sn and Nb present were in the form of mostly $SnO_2$ and $Nb_2O_5$ (XPS), Fig. K3, K4, K5. SIMS indicated that the $SnO_2$ was a thin surface layer ($\sim$18 Å) over further Nb oxides, Fig. K6. Short sputtering removed the $SnO_2$ and revealed a thick layer (between 36 and 159 Å) of Nb oxides and Na, Fig. K7. The maximum in the Na contamination occured at 36 Å. The initial secondary electron yield, $\delta$, of the $Nb_3Sn$ sample was high, due to this layer of adventitious carbon and oxides, Fig. K1. After sputter removal of the $SnO_2$ surface layer ($\sim$18 Å, using the sputter rate of Sn), $\delta$ dropped to esentially its final value for high incident energy, indicating that the beam was penetrating through the remaining non-$Nb_3Sn$ layer to the bulk material below. At low energy, however, $\delta$ was still elevated, due to surface contributions. This view is consistent with the appearance in the XPS core level of both oxide and metal components of Sn and Nb. SIMS showed mostly Nb oxide and Na at this point. After macro removal of $\sim 1\mu$ of material, the XPS

core levels reach their presumed (there is no information in the literature on this point) bulk values for $Nb_3Sn$. These are 202.85eV (vs. 202.0eV for metal) for the Nb component and 484.6eV (vs 484.45eV for the metal) for the Sn component.

The SIMS signal after 1$\mu$m of macro sputtering is shown in Fig. K8, and shows a very low value for Sn due to its high preferential sputtering yield. After the sample rested five days in vacuum, diffusion caused the Sn signal to rise, as shown in Fig. K9, indicating some surface rearrangement is occurring. H is clearly present in the bulk (SIMS) and the re-appearance of Nb and Sn oxides after sputtering would suggest that there is interstitial O available as well. This view is supported by the lack of $O_2$ and $H_2O$ in the residual gas of the analysis system. However, considering the strong affinity of Nb for water, the possible contamination of the sample from small amounts of gas phase $H_2O$ cannot be totally discounted, simply because the SIMS sensitivity for $H_2O$ is unknown and what appears to be a very small $H_2O$ peak was intermittently detected (by SIMS) on the sample surface when it was left in vacuum for several days at a time. As observed in the SIMS also, macro cleaned surfaces exhibit cluster ($Nb_2$, $Nb_3$, $Nb_4$...) behavior in the Nb and Nb oxide peaks. Oxidized surfaces, however, favor the appearance of NbO. Two other observations concerning SIMS are relevant here: 1) its sensitivity is very high for alkalis (hence the large K and Na peaks) and Al, and 2) the sputter yield for oxides of these species is much higher than for its non-oxide states (hence the much larger SIMS signals for oxidized surfaces). Included here for reference are measurements made at SLAC for anodized unsputtered $Nb_2O_5$ and sputter cleaned Nb, Fig. K10. The sputter cleaned $Nb_3Sn$ was also measured in the valence band (x-ray excited) and compares favorably with previously published results [Höchst (1976)]; both are shown in Fig. K11. Finally, no evidence of Cl, or contaminants other than those mentioned already, could be found by AES, XPS, or SIMS.

In summary, this sample appears to be $Nb_3Sn$ bulk-contaminated with H and possibly O. The as-received sample structure was identified as: several Å of C, $SnO_2$ and $Nb_2O_5$; 18 Å of $SnO_2$; 36 to 159 Å of Nb oxides and Na; remainder $Nb_3Sn$. Re-oxidation of the Nb and Sn components (for the clean $Nb_3Sn$ surface)

occurs after several days in vacuum, but the source of the oxidant is not firmly established. Apparently the sample, after deposition, was contaminated by a Na source (perhaps a breath?) after which it naturally oxidized in air. During handling and shipping it acquired a hydrocarbon adlayer (completely normal and unavoidable). The $Nb_3Sn$ seems to acquire a $SnO_2$ outer layer both in the as-received and sputter-cleaned states. In the as-received sample, this $SnO_2$ layer is apparently below the C, suggesting that it occurred well before (and perhaps, even retarded) the subsequent hydrocarbon contamination.

## 4. Directions for Future Surface Physics Research

1. At SLAC, we will explore feasibility of making continuous coatings of Y or Al on (rough) cavity surfaces, and of subsequently forming continuous non-oxidizing films of relatively inert metals such as Pt or Rh over the reactive metal layer. We will examine oxidation behavior, secondary emission, and field emission behavior before and after breakdown.

2. We all await with interest results from the field emission scanning facility with $1\mu m$ resolution which has been constructed in O. Fischer's laboratory at the University of Geneva. With its coupled scanning Auger equipment, information on emission site distribution and composition should be forthcoming, which should point the direction toward reducing the number and effect of such sites.

3. The spectrum of light emitted from "glowing" cavities should be investigated to discriminate between $e^-$ luminescence and thermal radiation, in order to illuminate the role of unified temperature-field emission.

## Acknowledgments

I thank the many individuals and groups who furnished me with preprints and information on their research. I am particularly grateful to my secretary Arla LeCount and the personnel of the SLAC Reports office for their yeoman service on my behalf.

## References


4. G. Arnolds-Mayer and N. Hilleret (1982), "Field Emission and Secondary Electron Emission from $Nb_3Sn$ Surfaces", Adv. in Cryogenic Engin. Materials 28, 611 (1982).

5. J. Bermond (1975), "A Measurement of the Local Electric Field on Field Emitter Crystals Using *T-F* Emission", Surf. Sci. 50, 311-328 (1975).

6. J. Bermond, M. Lenoir, J. Prulhiere and M. Drechsler (1974), "Numerical Data and Experimental Proof of the Unified Theory of Electron Emission (Christov)", Surf. Sci. 42, 306-323 (1974).

7. G. Betz and G. Wehner (1983), "Sputtering of Multi-Component Materials", in Topics in Applied Physics, ed. by R. Behrisch [Springer, Berlin (1983)] V.52.

8. I. Bronshtein and S. Denisov (1965), "Effect of the Work Function on Parameters of Secondary Electron Emission", Sov. Phys.-Solid State 6, 1515 (1965).

9. I. Campisi, H. Deruyter, Z. Farkas, E. Garwin, H. Hogg, F. King, and R. Kirby (1983), "RF Superconducting Properties of Thin Films on Niobium", IEEE Trans. Nucl. Sci. NS-30, 3363 (1983).

10. S. Christov (1966), "General Theory of Electron Emission from Metals", Phys. Stat. Sol. 17, 11 (1966).

11. S. Christov (1967), "Unified Theory of Thermionic and Field Emission from Semiconductors", Phys. Stat. Sol. 21, 159 (1967).

12. S. Christov (1969), "Injected Electron Currents Through Insulators", Phys. Stat. Sol. 32, 509 (1969).

13. S. Christov (1971), "Theory of Electron Emission into Dielectrics with Arbitrary Band Structure", Phys. Stat. Sol. (a) 7, 371 (1971).

14. S. Christov (1973), "Electron Currents Across Metal-Semiconductor Interfaces", Phys. Stat. Sol. (a) 15, 665 (1973).

15. S. Christov (1978), "Recent Test and New Applications of the Unified Theory of Electron Emission", Surf. Sci. 70, 32-51 (1978).

16. G. Dominichini and N. Hilleret (1984), "Influence de traitements par decharge gazeuse sur l'emission electronique du niobium", CERN NOTE TECHNIQUE LEP/VA/nh, 22 Feb. 1984.

17. E. Garwin, R. Kirby, E. Hoyt, and T. Momose (1981), "Electron Activated Carbon Diffusion in Niobium Compounds for RF Superconductivity", SLAC-PUB 2716, March (1981) and extended abstract in Vacuum 31, 597 (1981).

18. J. Gibson and R. Thomas (1982), "Secondary Electron Emission and Conductivity Mechanisms of Epitaxial MgO Films", Appl. Surf. Sci. 14, 56 (1982).

19. M. Grundner and J. Halbritter (1980 A), "XPS and AES Studies on Oxide Growth and Oxide Coatings on Niobium", J. Appl. Phys. 51, 397 (1980).

20. M. Grundner and J. Halbritter (1980 B), "On Surface Coatings and Secondary Yield of $Nb_3Sn$ and Nb", J. Appl. Phys. 51, 5396 (1980).

21. M. Gurvitch and J. Kwo (1984), "Advances in Cryogenic Engineering" v. 30 (Materials), Proc. of the 1983 Int'l Cryogenic Mat'ls Conf., Plenum Press, N.Y., (to be publ. 1984).

22. J. Halbritter (1981), "On Residual RF Losses and Tunnel Currents Caused by Interface States", IEEE Trans. Magnetics MAG-17, 943 (1981).

23. J. Halbritter (1982), "Weakening of Superconducting Interaction at Nb-$Nb_2O_5$ Interfaces", Proc. IV Conf. on Supercond. in d- and f-band Metals, June 1982, Karlsruhe.

24. J. Halbritter (1984 A), "On RF Residual Losses in Superconducting Cavities", Proc. 2nd Workshop on RF Superconductivity, CERN, 23-27 July 1984.

25. J. Halbritter (1984 B), "On Changes of Secondary Emission by Resonant Tunneling via Adsorbates", Jour. de Physique 45, C2-315 (1984).

26. J. Hauser, D. Bacon, and W. Haemmerle (1966), "Energy Gap of $V_3Si$", Phys. Rev. 151, 296 (1966).

27. H. Höchst, S. Hüfner and A. Goldmann (1976), "XPS Valence Band Spectra of $Nb_3Sn$, Nb and Sn", Solid State Comm., 19, 899 (1976).

28. P. Karulkar (1981), "Effects of Sputtering on the Surface Composition of Niobium Oxides", J. Vac. Sci. Technol., 18, 169 (1981).

29. U. Klein and J. Turneaure (1983), "Field Emission in Superconducting RF Cavities", IEEE Trans. Magn. MAG-19, 1330 (1983).

30. T. Lin and D. Lichtman (1979), "Electron Irradiation Effects on Oxidized Nb Foil and NbO", J. Mat. Sci. 14, 455 (1979).

31. J. Miller, I. Lindau, P. Stefan, D. Weissman, M. Shek and W. Spicer (1982 A), "Photoemission Studies of Clean and Oxidized Nb and $Nb_3Sn$", J. Appl. Phys 53, 3267 (1982).

32. J. Miller, I. Lindau, and W. Spicer (1982 B), "A Photoemission Study of Clean and Oxidized $Nb_3Sn$", Phys. Lett. 88A, 97 (1982).

33. M. Oshima, B. Pate, Z. Lu, P. Jupiter, I. Lindau, and W. Spicer (1983), "Photoemission Studies of a Clean and Oxidized Nb-Al Alloy Using Synchrotron Radiation", Solid State Commun. 46, 815 (1983).

34. H. Padamsee (1984), "Technology of Nb Production and Purification", 2nd Workshop on RF Superconductivity, Geneva, 23-27 July, 1984.

35. H. Padamsee, M. Banner, and M. Tigner (1977), "Suppression of Multipactoring in SC Cavities", IEEE Trans. Nucl. Sci., NS24, 1101 (1977).

36. P. Pianetta, I. Lindau, C. Garner, and W. Spicer (1978), "Chemisorption and Oxidation Studies of the (110) Surfaces of GaAs, GaSb, and InP", Phys. Rev. B, 18, 2792 (1978).

37. P. Reader and H. Kaufman (1975), "Optimization of an Electron-Bombardment Ion Source for Ion Machining Applications", J. Vac. Sci. Technol. 12, 1344 (1975).

38. F. Rohrbach (1971), Title Unknown, CERN/TC/L 71-5 (1971).

39. A. Septier (1980), "Surface Studies and Electron Emissions", Proc. Workshop of RF Supercond., ed. by M. Kuntze, Karlsruhe July 2-4, 1980, Report KfK 3019.

40. D. Smathers and D. Larbalestier (1980), "An Auger Electron Spectroscopy Study of Bronze Route Niobium-Tin Diffusion Layers", in Filamentary A15 Superconductors, p. 143, ed. by M. Suenaga and A. Clark, Plenum Press, N.Y. (1980).

41. L. Toth (1971), Transition Metal Carbides and Nitrides Academic Press, N.Y. (1971).

42. G. Wehner (1982), "Sputtering of Multicomponent Materials", J. Vac. Sci. Technol. A1, 487 (1982).

43. M. Wittmer, J. Noser and H. Melchior (1981), "Oxidation Kinetics of TiN Thin Films", J. Appl. Phys. 52, 6659 (1981).

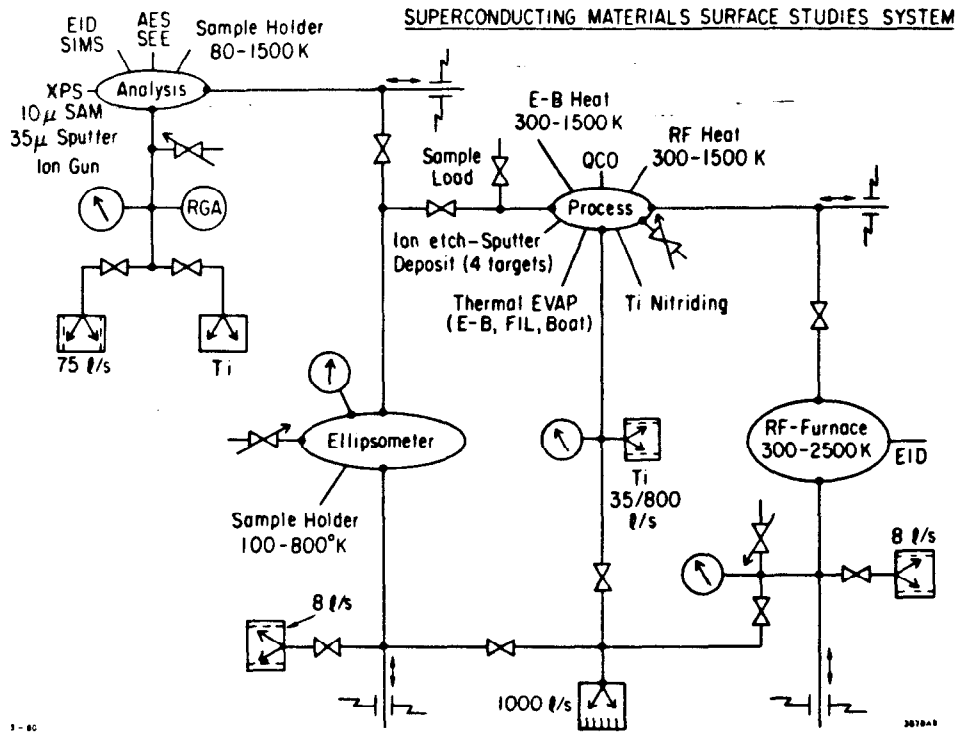


**Figure 1**

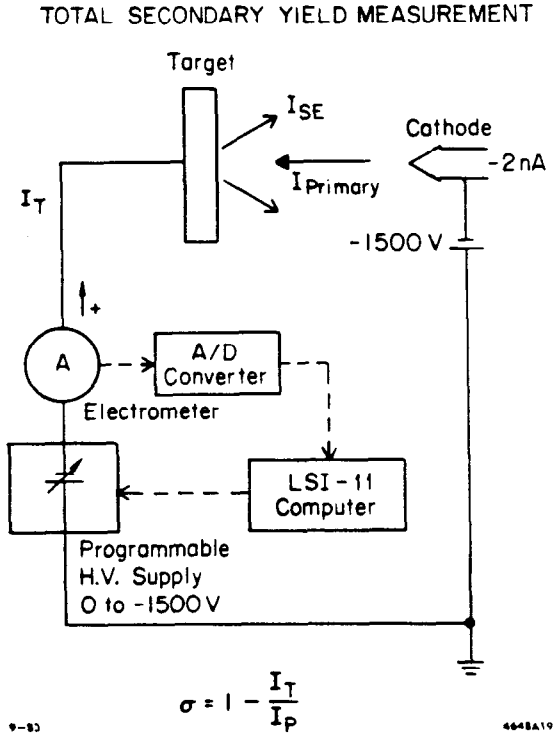


**Figure 2**

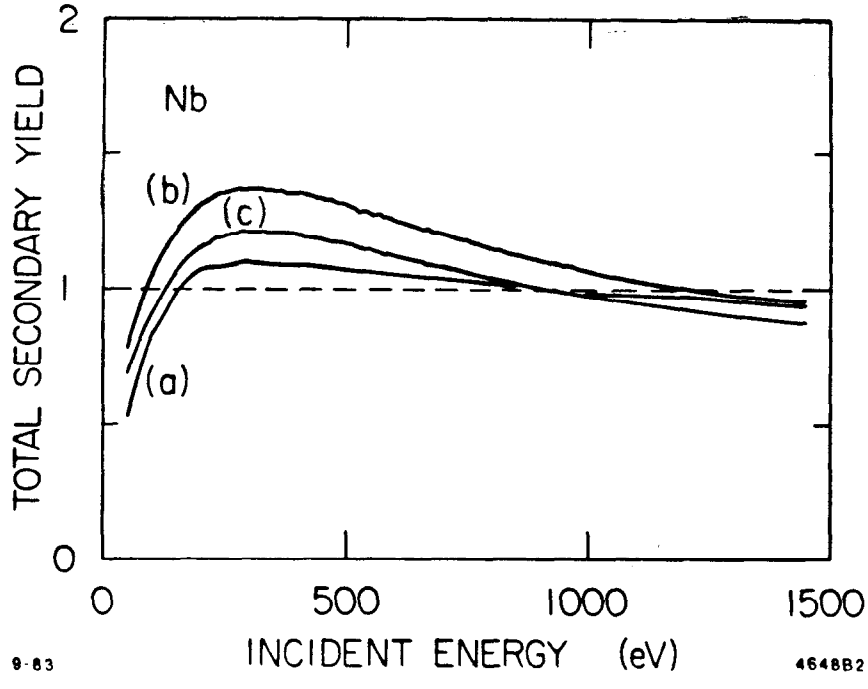


Figure 3

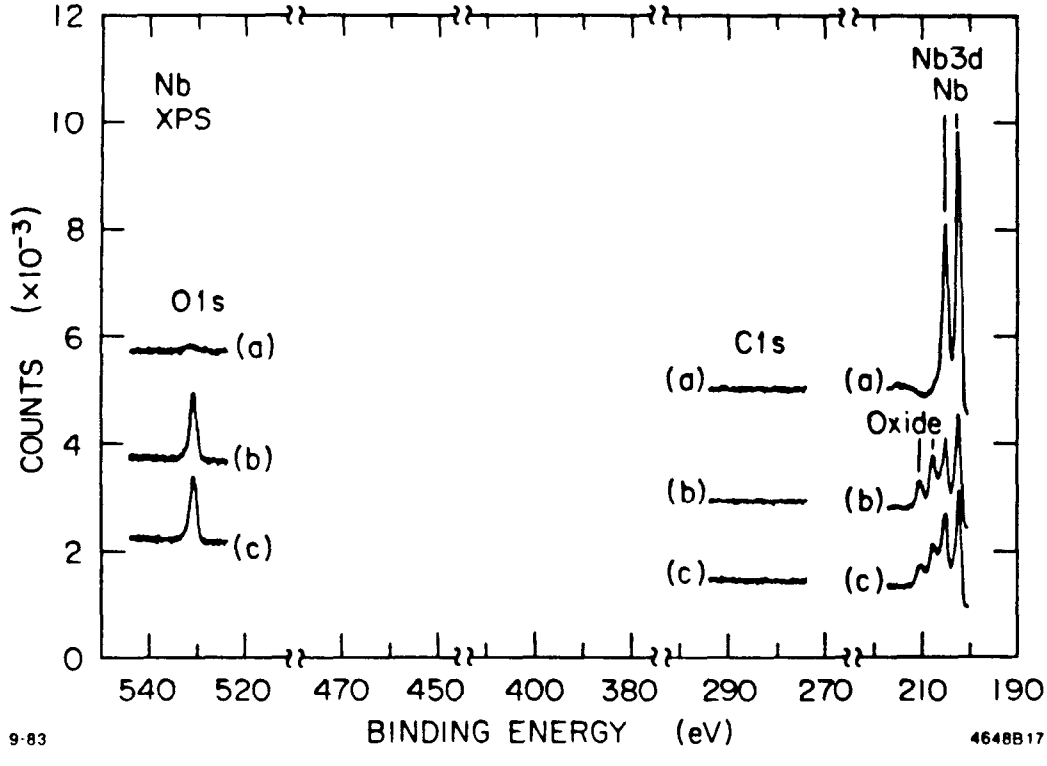


Figure 4

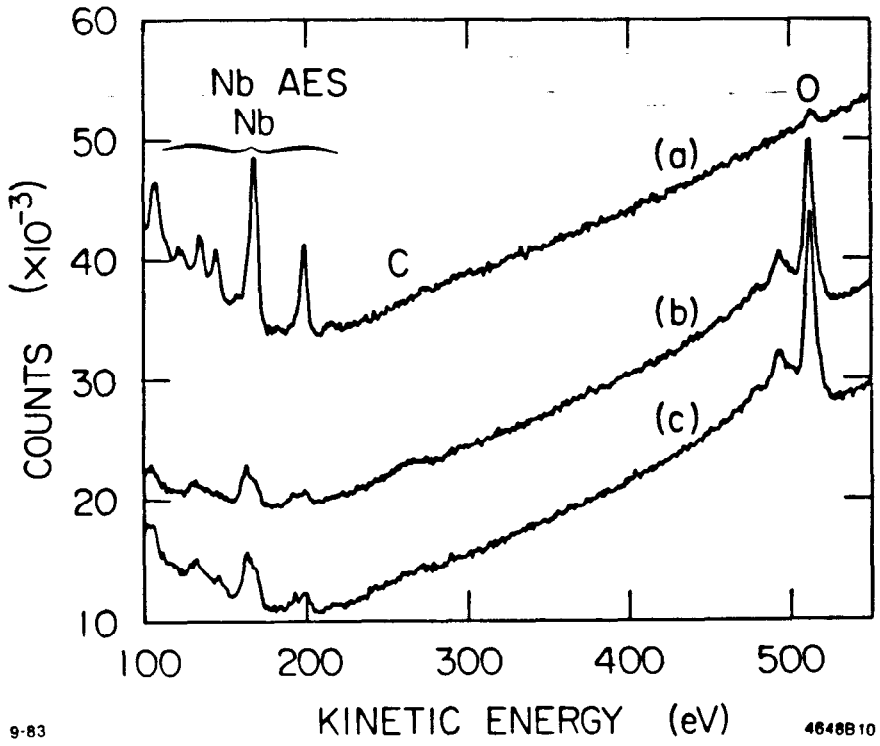


Figure 5

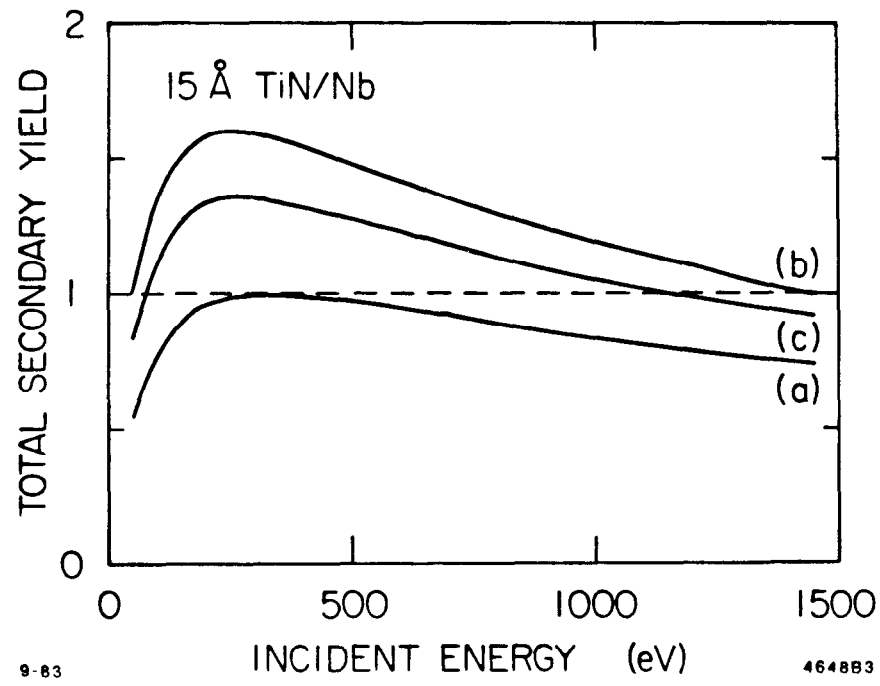


Figure 6

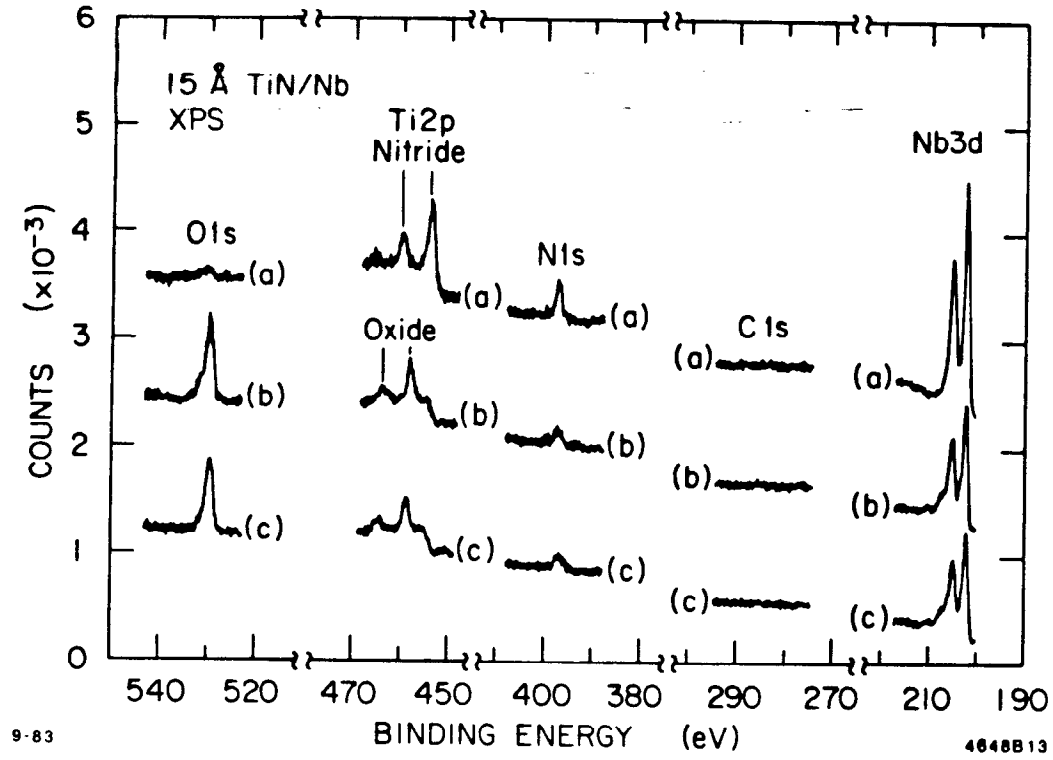


Figure 7

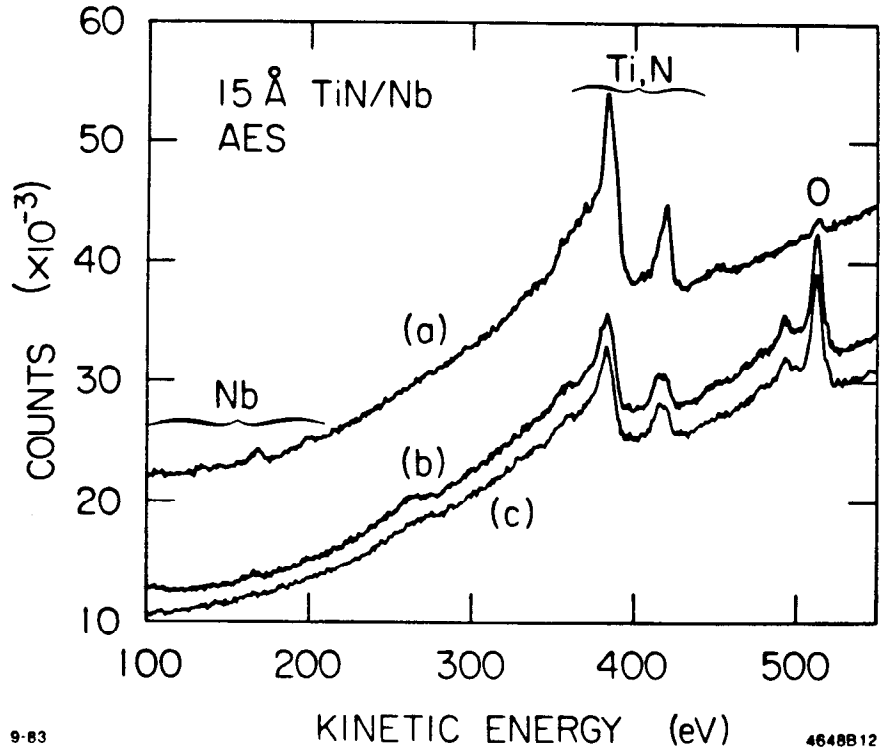


Figure 8

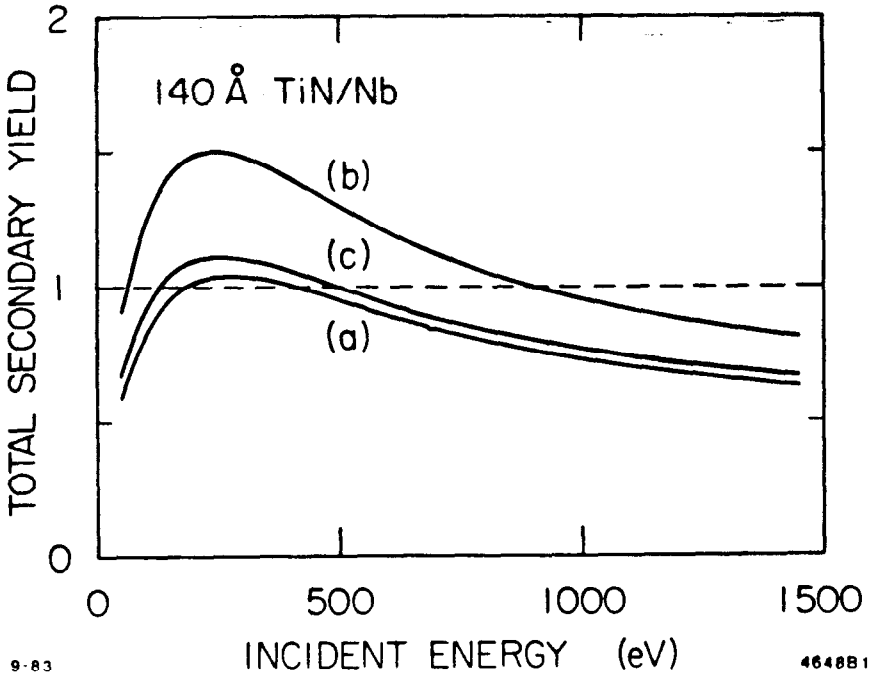


Figure 9

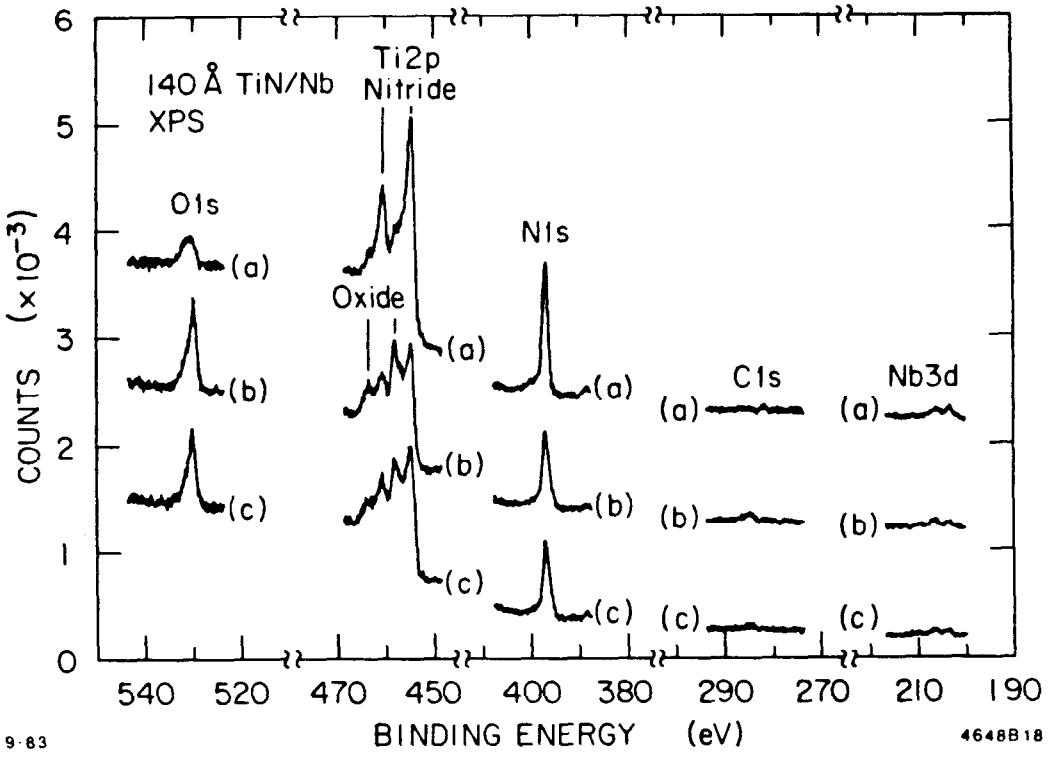


Figure 10

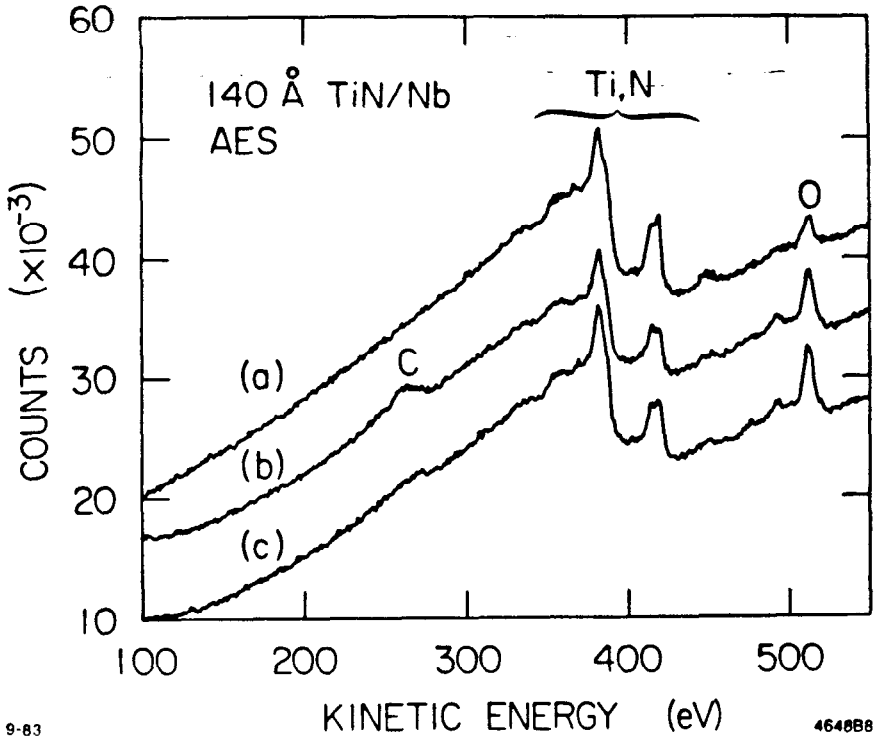


Figure 11

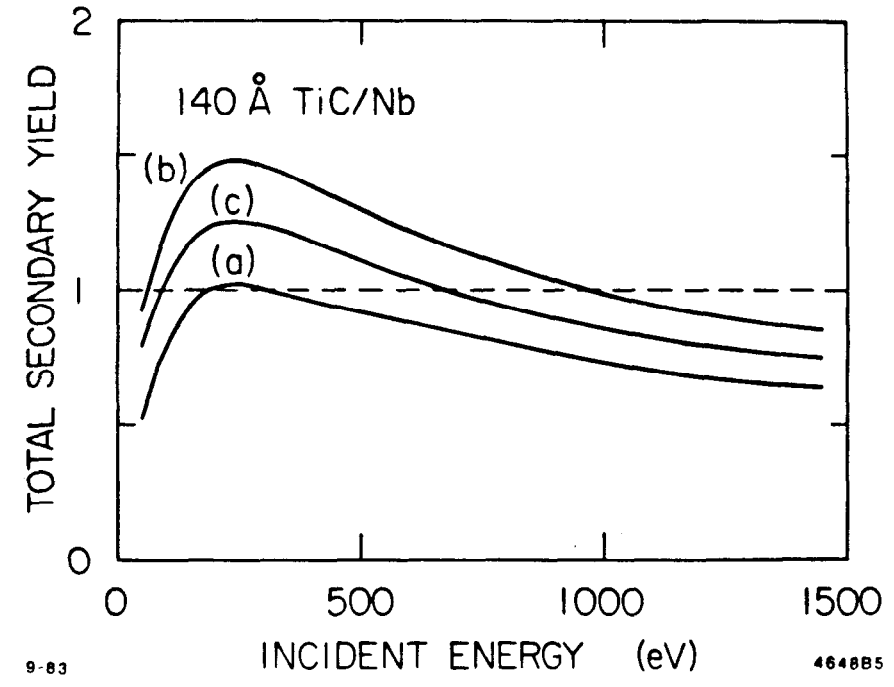


Figure 12

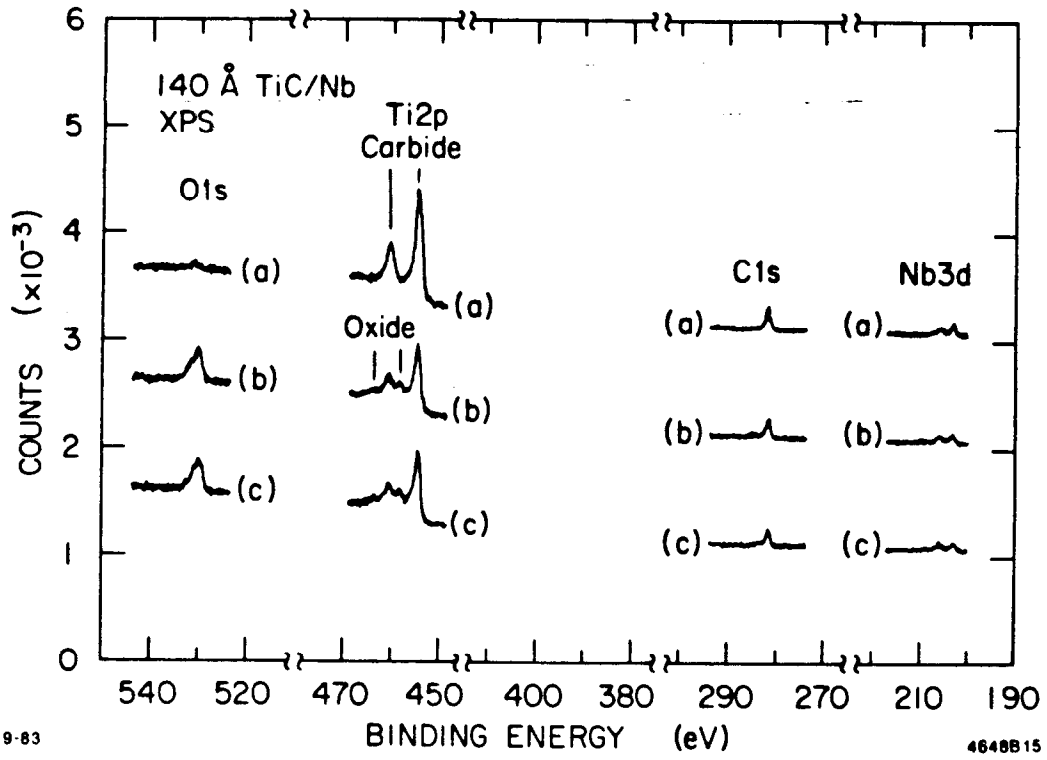


Figure 13

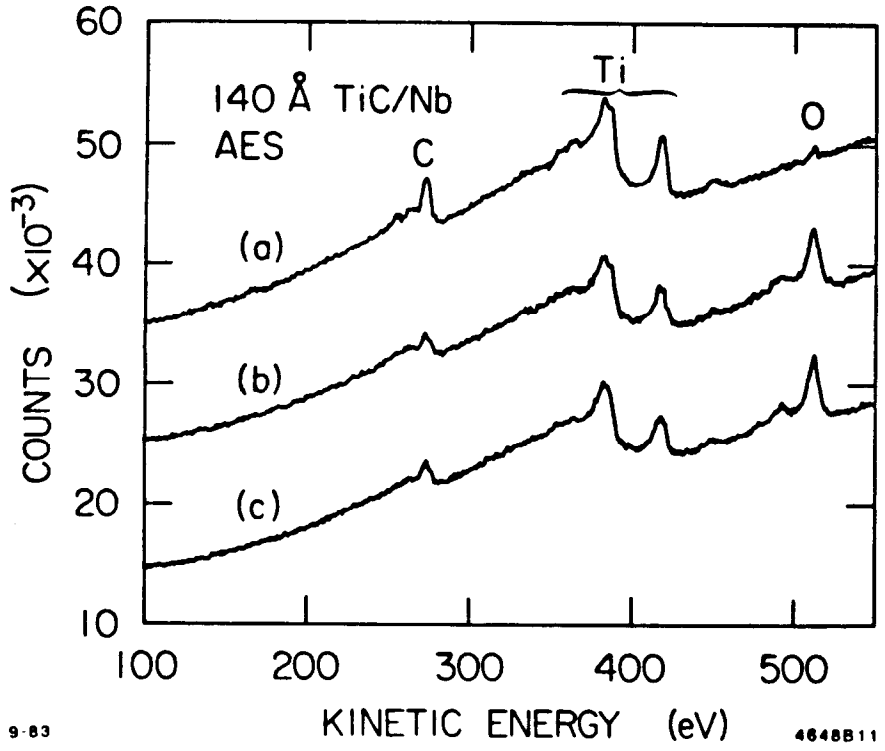


Figure 14

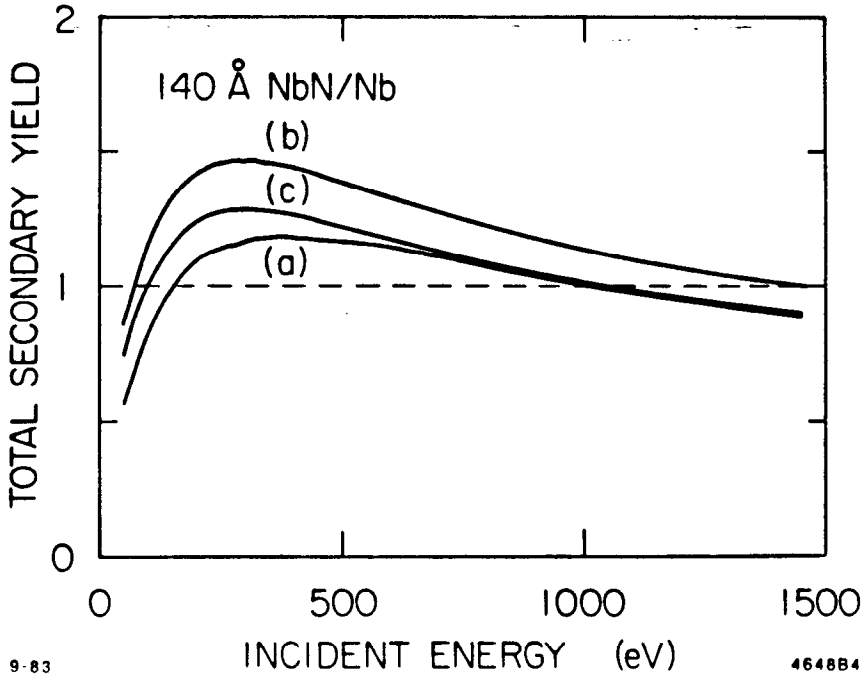


Figure 15

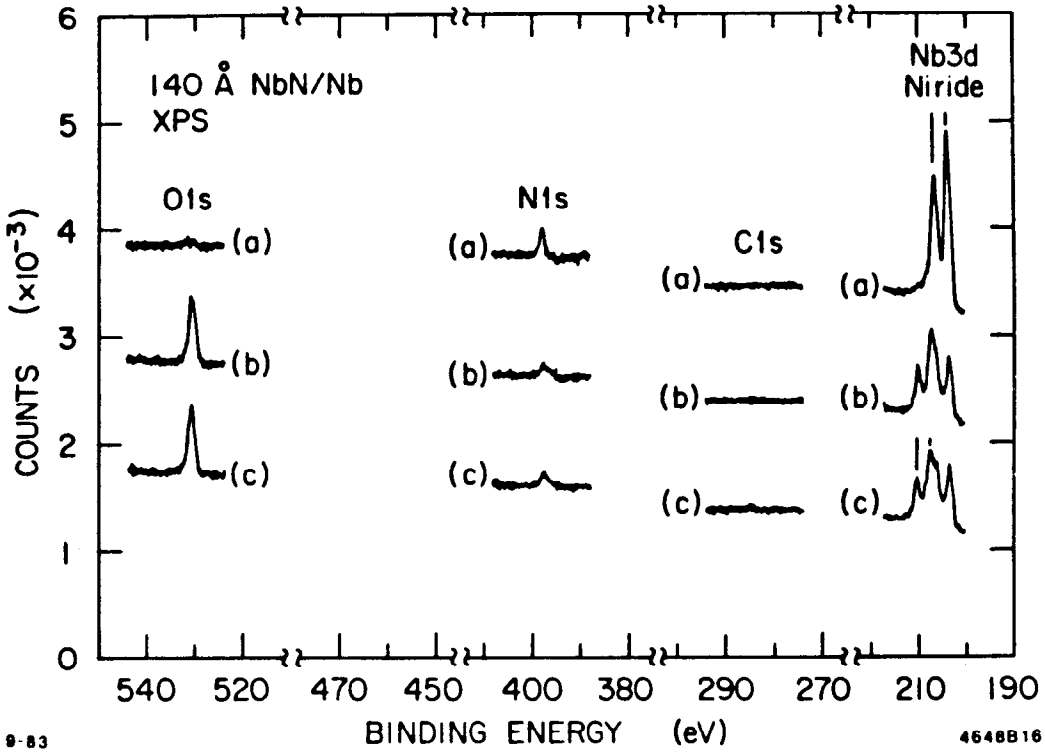


Figure 16

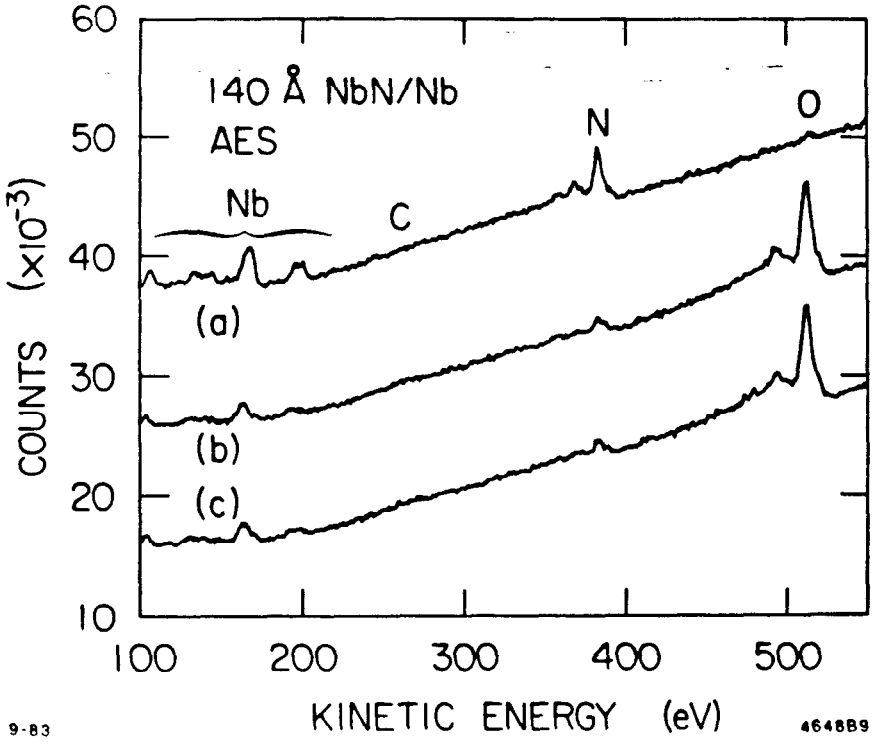


Figure 17

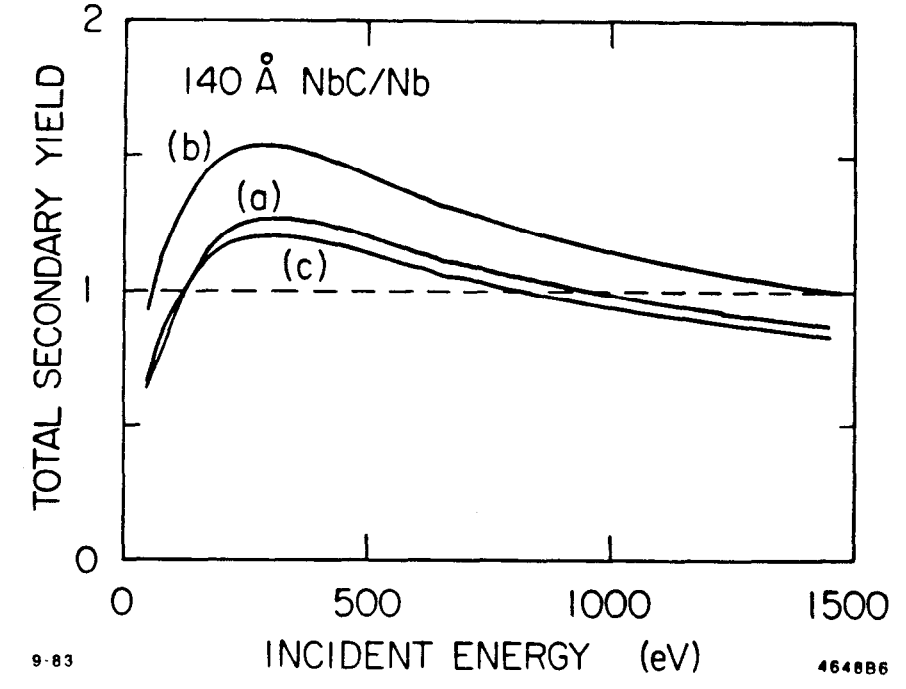


Figure 18

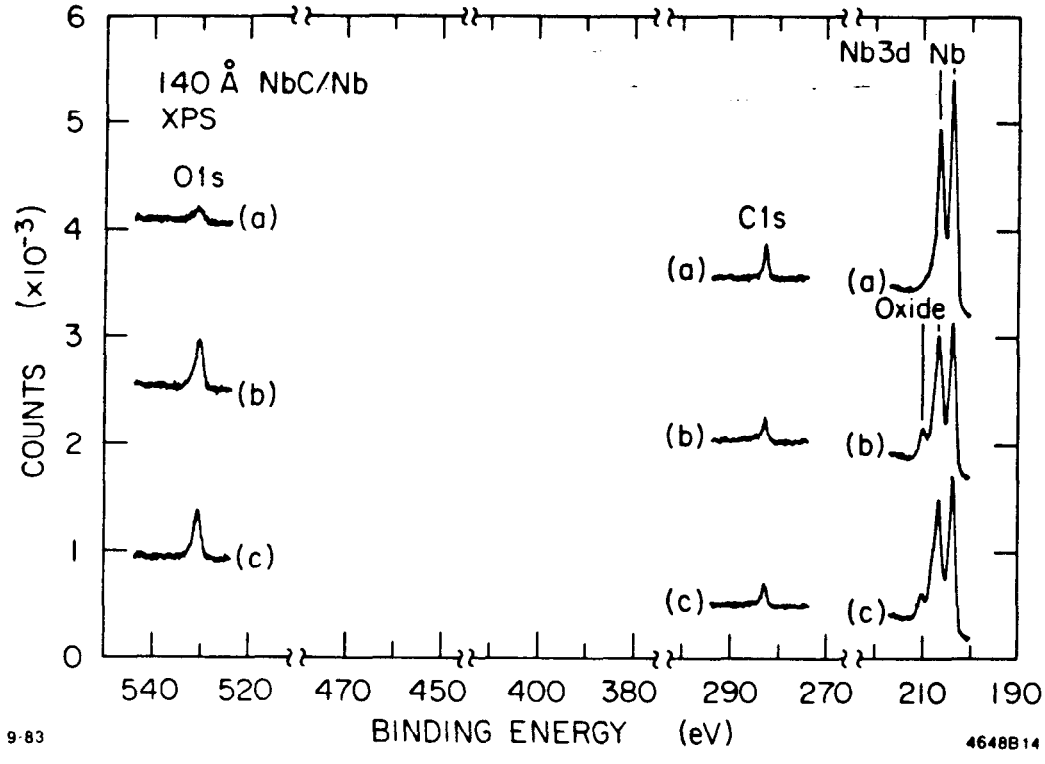


Figure 19

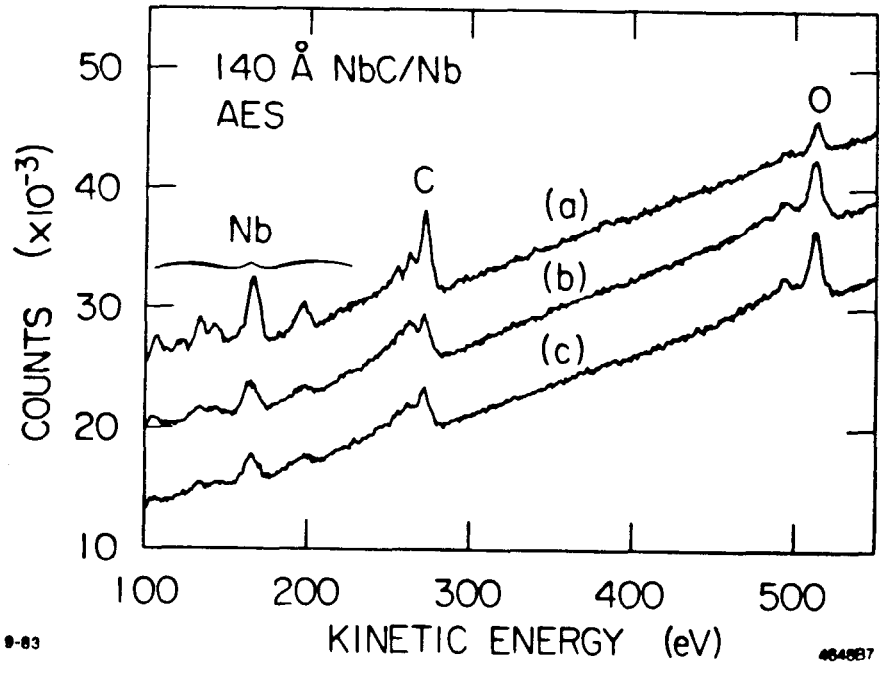


Figure 20

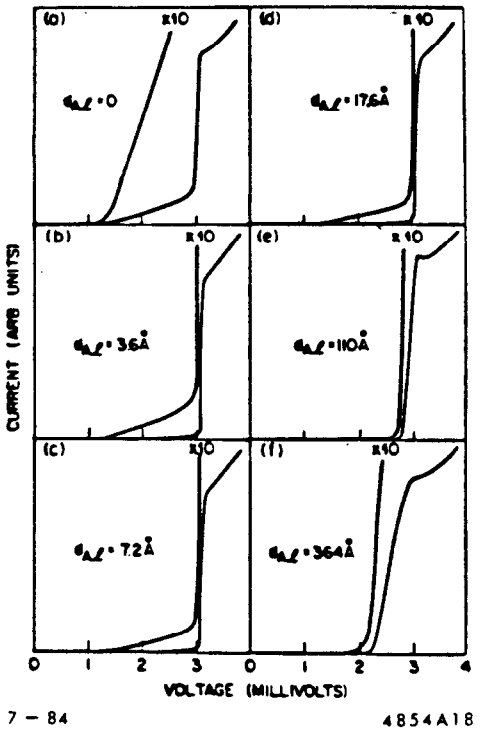


Fig. G4 Characteristics of $Nb/A\ell$ - oxide - $Pb_{0.90}Bi_{0.10}$ Junctions with Different $d_{A\ell}$ at $T = 2°K$.

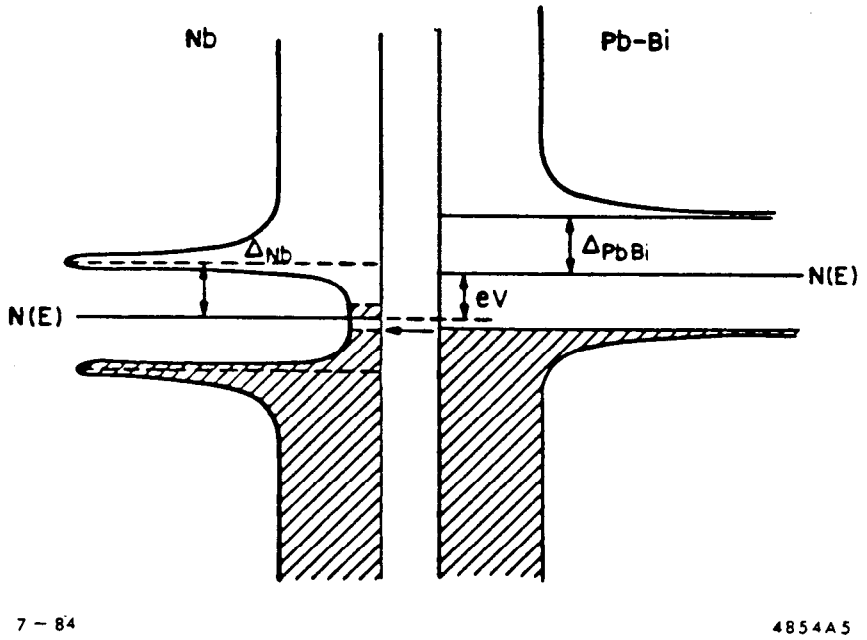


Fig. G6 Tunneling Diagram showing clean gap in $PbBi$ and tail in the $Nb$ density of states.

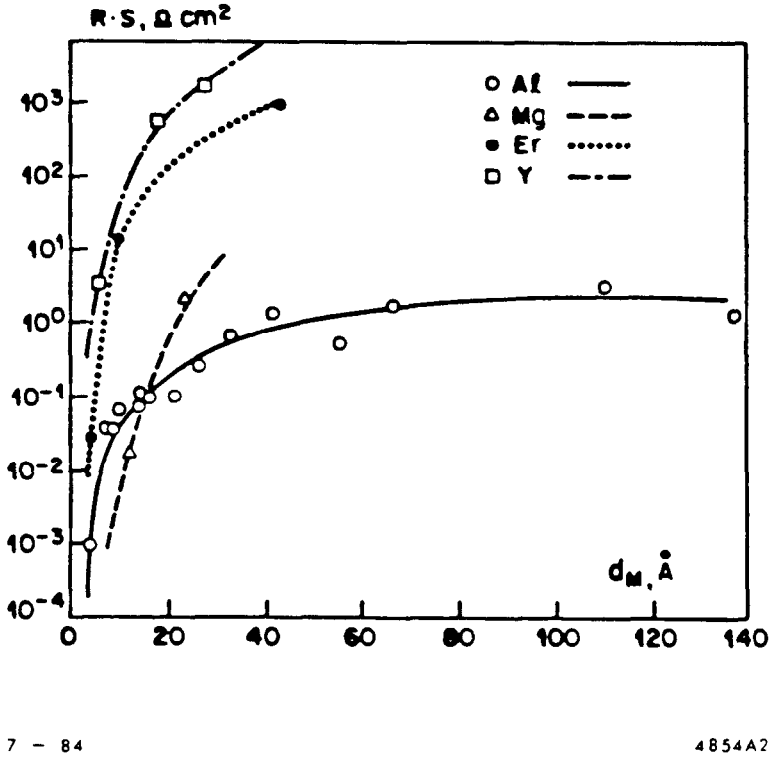


Fig. G10 Oxide tunneling resistance of broad area junctions as a function of $d_M$; $T = 77°K$.

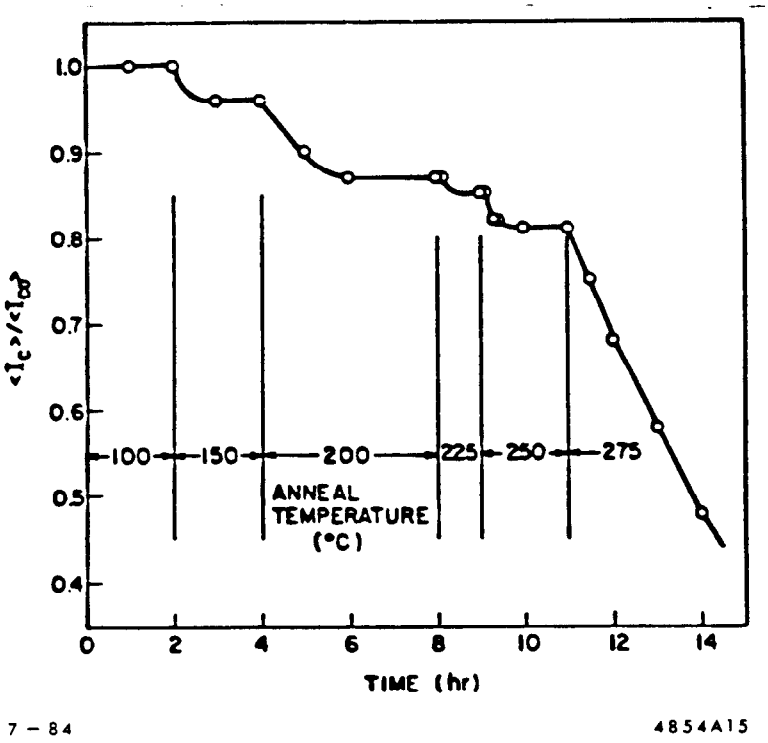


Fig. G11 Behavior of the average critical current at different annealing temperatures.

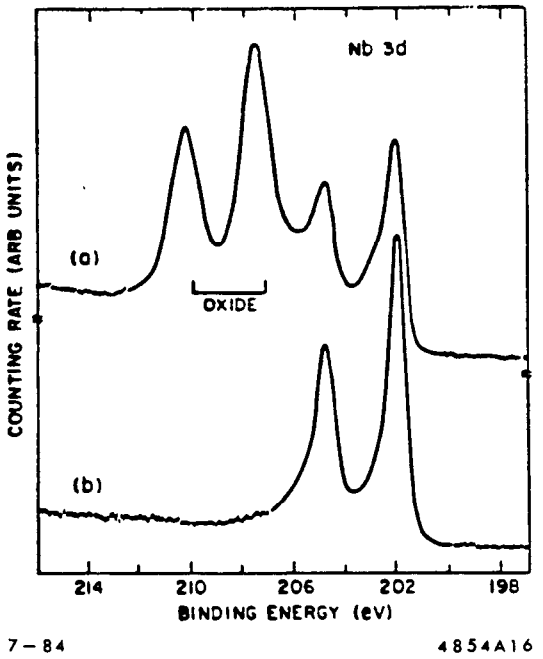


Fig. G12 *XPS Nb3d* a) Air-oxidized *Nb* film, b) air-oxidized *Nb/Aℓ* (38.5 Å).

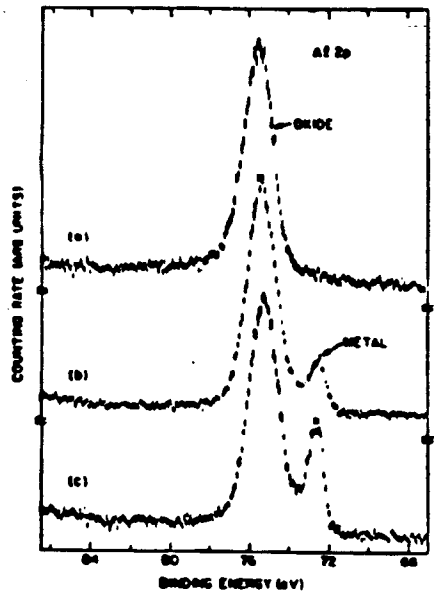


Fig. G13 *XPS* $A\ell^2$ *p* of air oxidized *Nb/Aℓ* with nominal $d_{A\ell}$ = a) 9.5 Å; b) 38.5 Å and c) 112 Å.

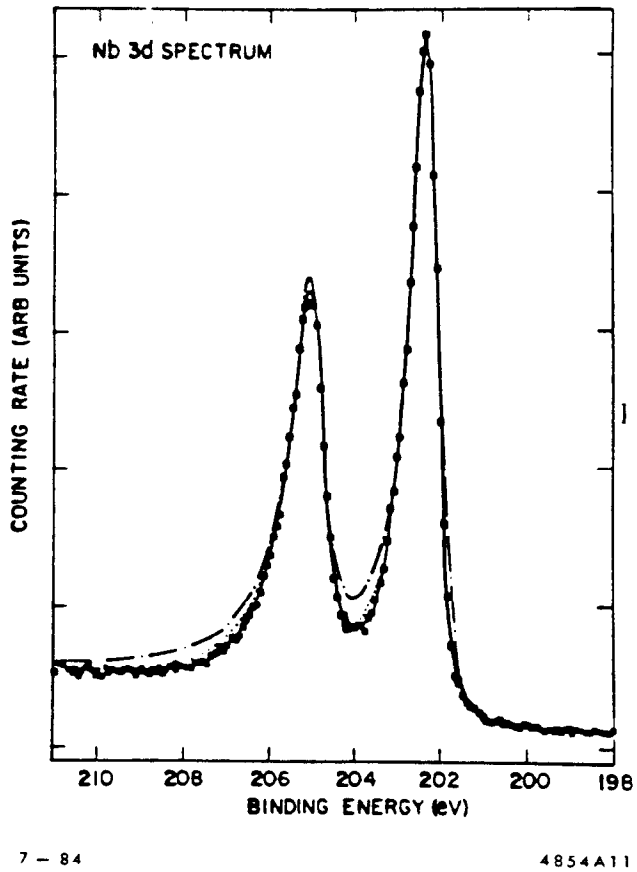


Fig. G14 *XPS Nb 3d* (—) scraped in situ at $7 \times 10^{-7}$ Torr, (. . . .) 15 min. after in situ scraping at $10^{-9}$ Torr, (— · — · —) *Nb/Aℓ* (112 Å) over layer structure.

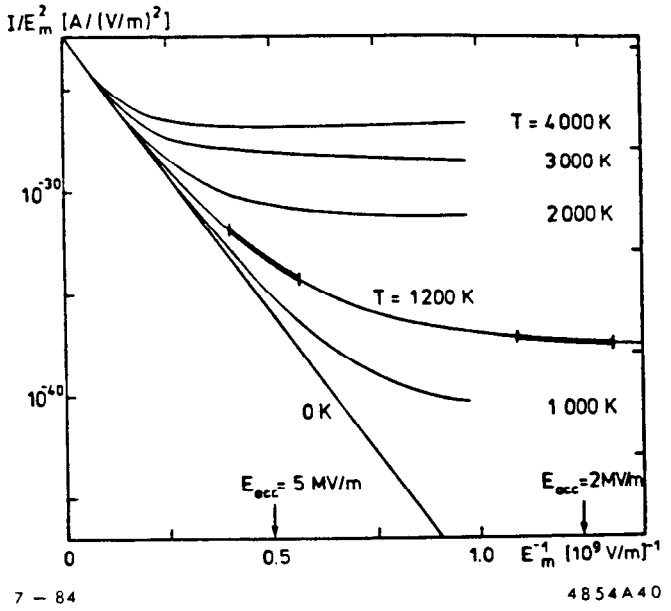


Fig. KT6 Field emission characteristic of a typical emitter ($\beta = 200$) for different temperatures $T$. $E_m$ is the microscopic electric field at the emitter. For an accelerating cavity with peak field ratio of 2 the arrows indicate two values of the accelerating field. Depending on the field interval where field emission is observed the field emission theory for $T = 0\ K$ yields completely different $\beta'$-values if $T \gg 0\ K$.

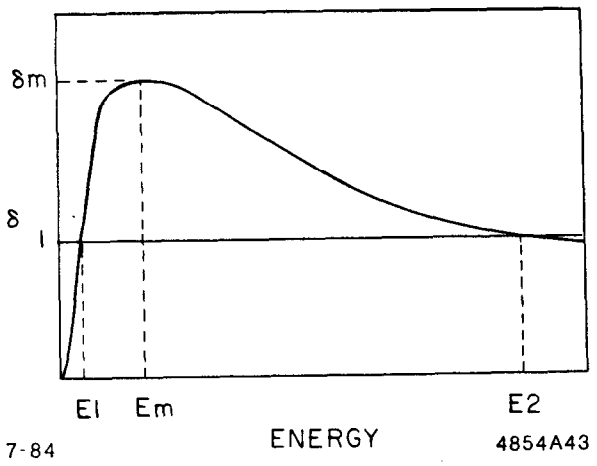


Fig. DH11 Secondary Emission Coefficient, $\delta$, vs Energy of Incident Electrons.

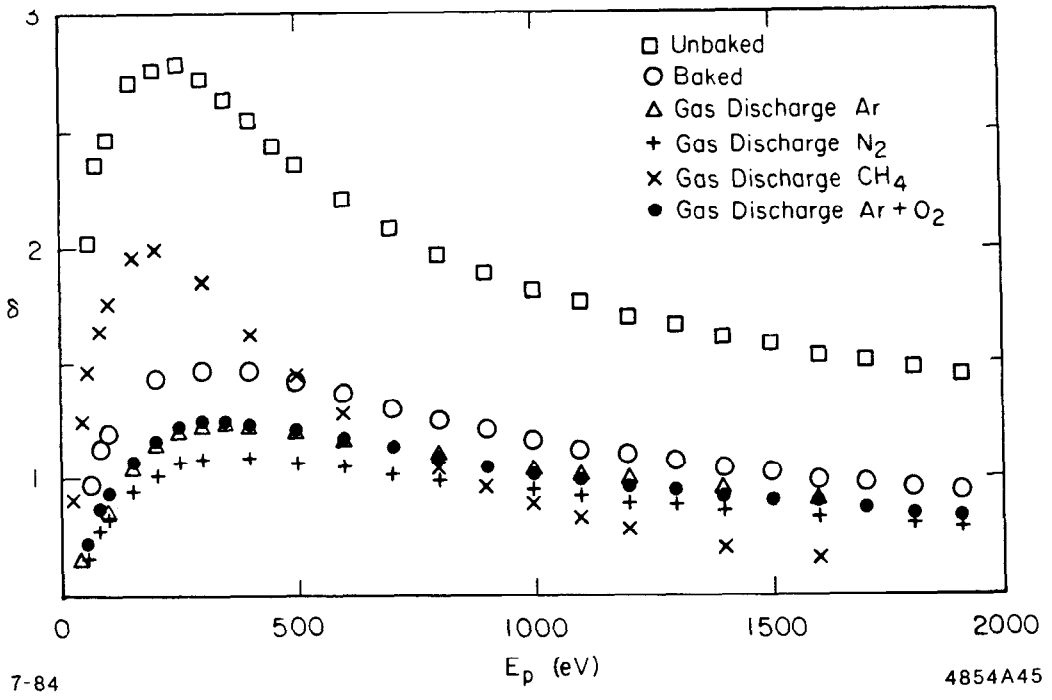


Fig. DH12 $\delta$ vs Incident Electron Energy for Different Surface Treatments.

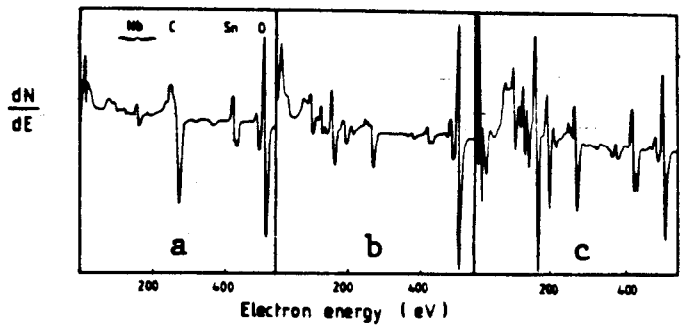


Fig. A-M3 Auger Spectra a) as received, b) after 1 min. AGD, c) after complete removal of the oxide layer.

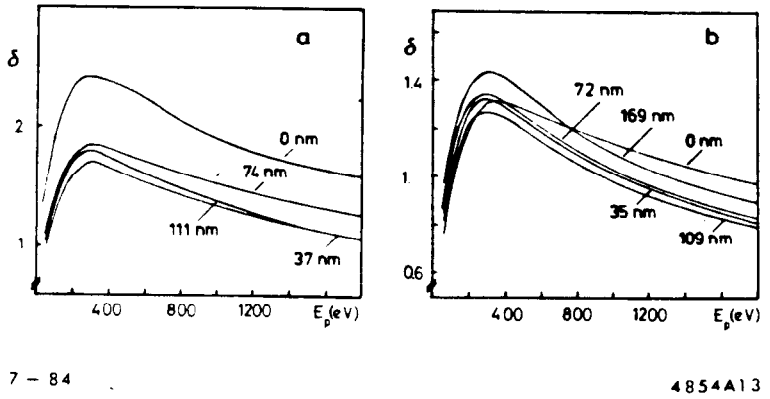


Fig. A-M4 Secondary electron yields of anodized $Nb_3Sn$ a) as received, b) after 1 min. AGD.

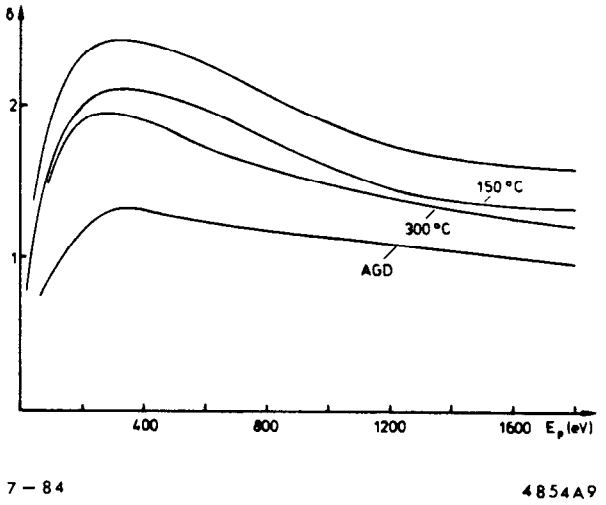


Fig. A-M5 Secondary electron yields of $Nb_3Sn$.

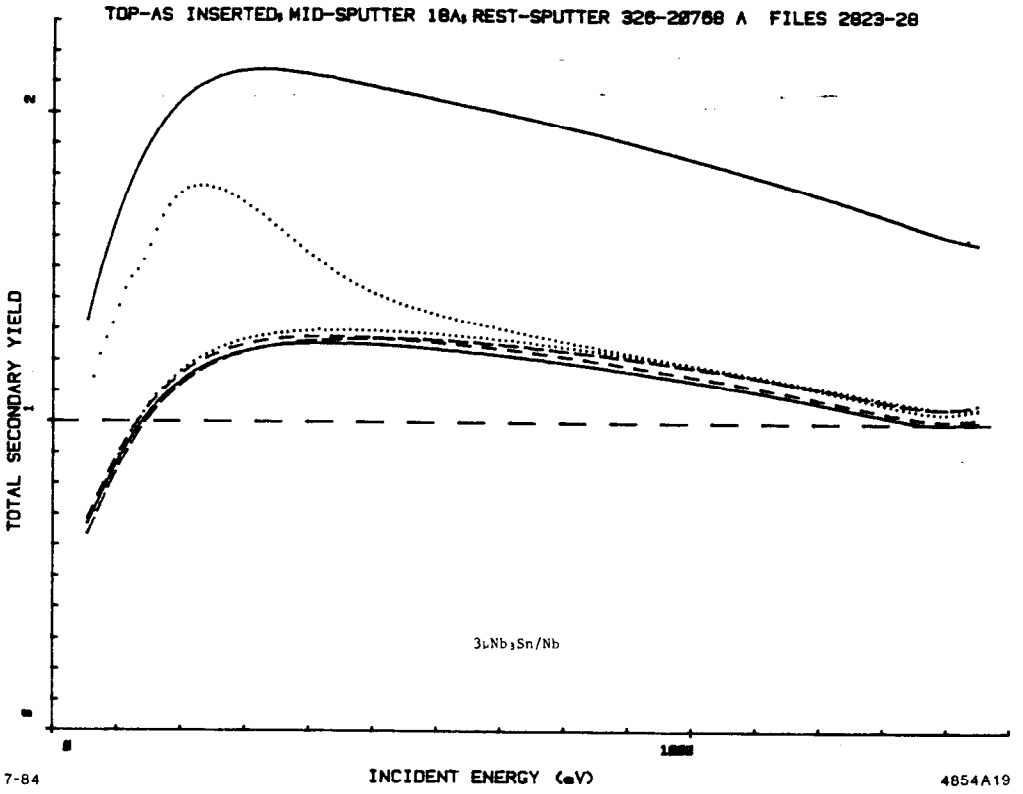


Fig. K1

AES

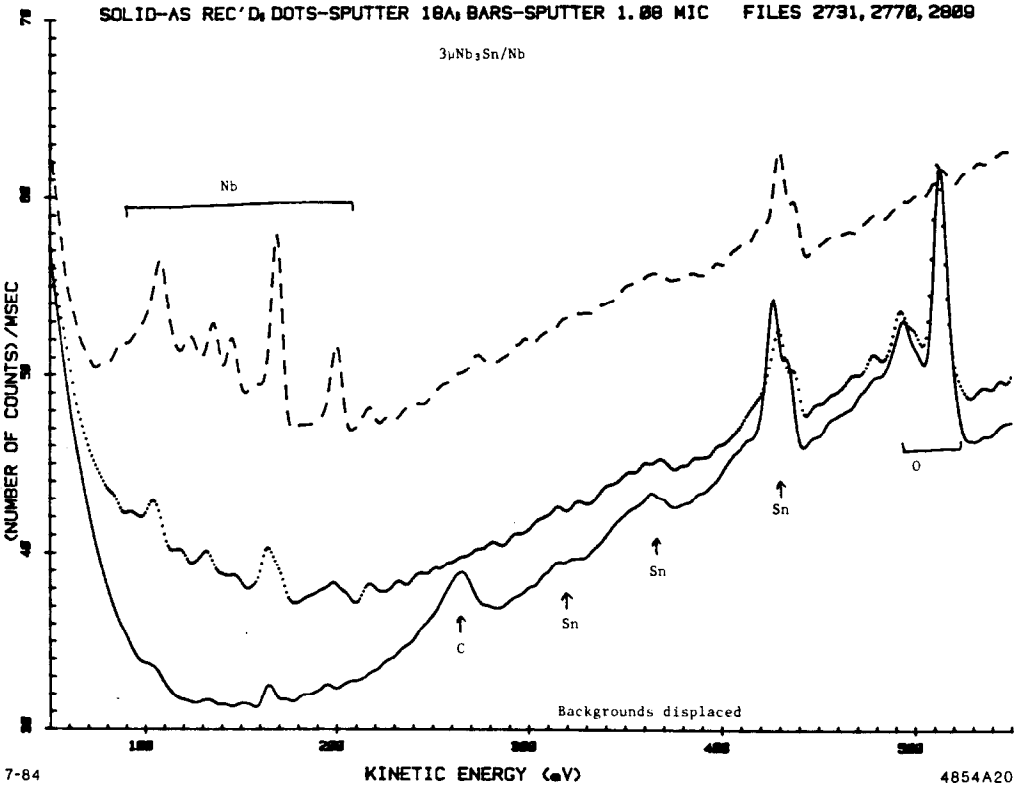


Fig. K2

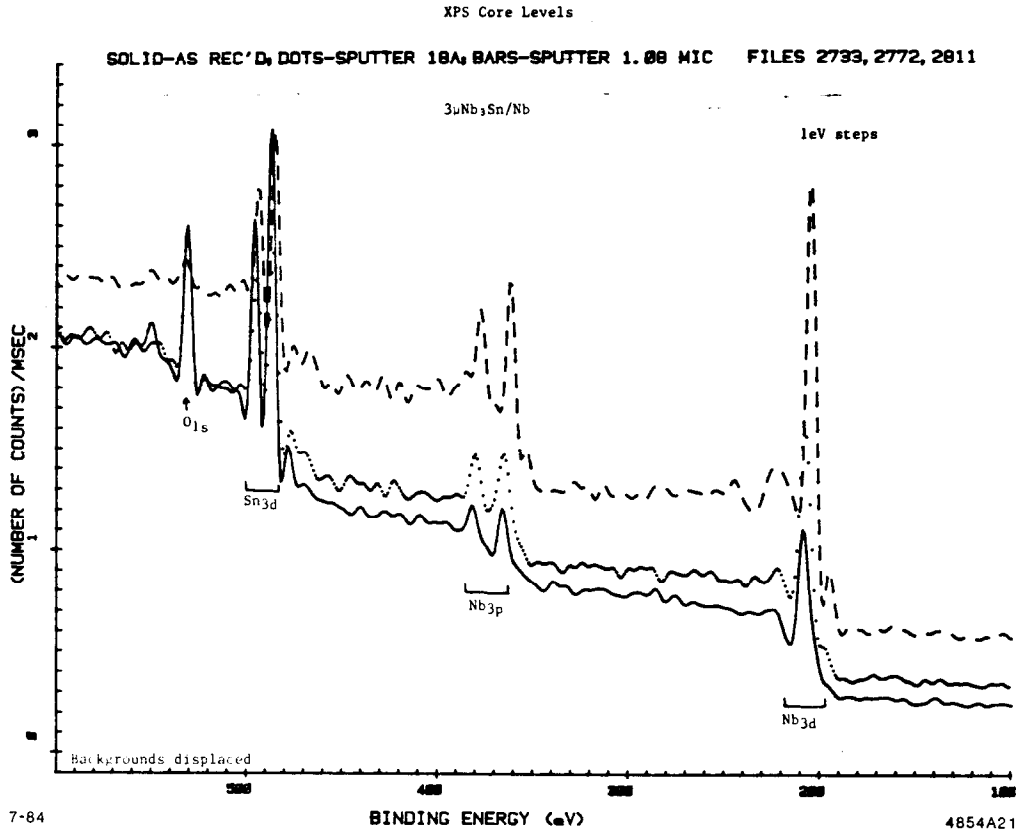
XPS Core Levels
SOLID-AS REC'D, DOTS-SPUTTER 18Å, BARS-SPUTTER 1.00 MIC FILES 2733, 2772, 2811
3μNb3Sn/Nb
1eV steps
(NUMBER OF COUNTS)/MSEC
O1s
Sn3d
Nb3p
Nb3d
Backgrounds displaced
BINDING ENERGY (eV)
7-84
4854A21

Fig. K3

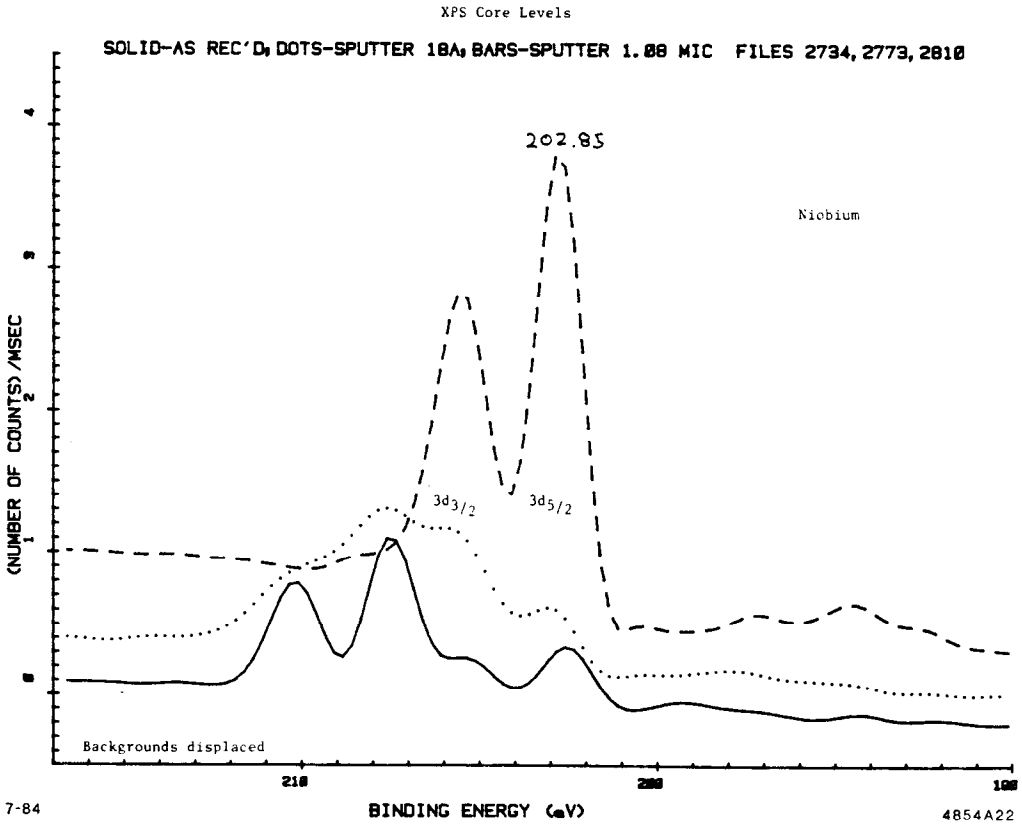
XPS Core Levels
SOLID-AS REC'D, DOTS-SPUTTER 18Å, BARS-SPUTTER 1.00 MIC FILES 2734, 2773, 2810
202.85
Niobium
(NUMBER OF COUNTS)/MSEC
3d3/2
3d5/2
Backgrounds displaced
BINDING ENERGY (eV)
7-84
4854A22

Fig. K4

XPS Core Levels

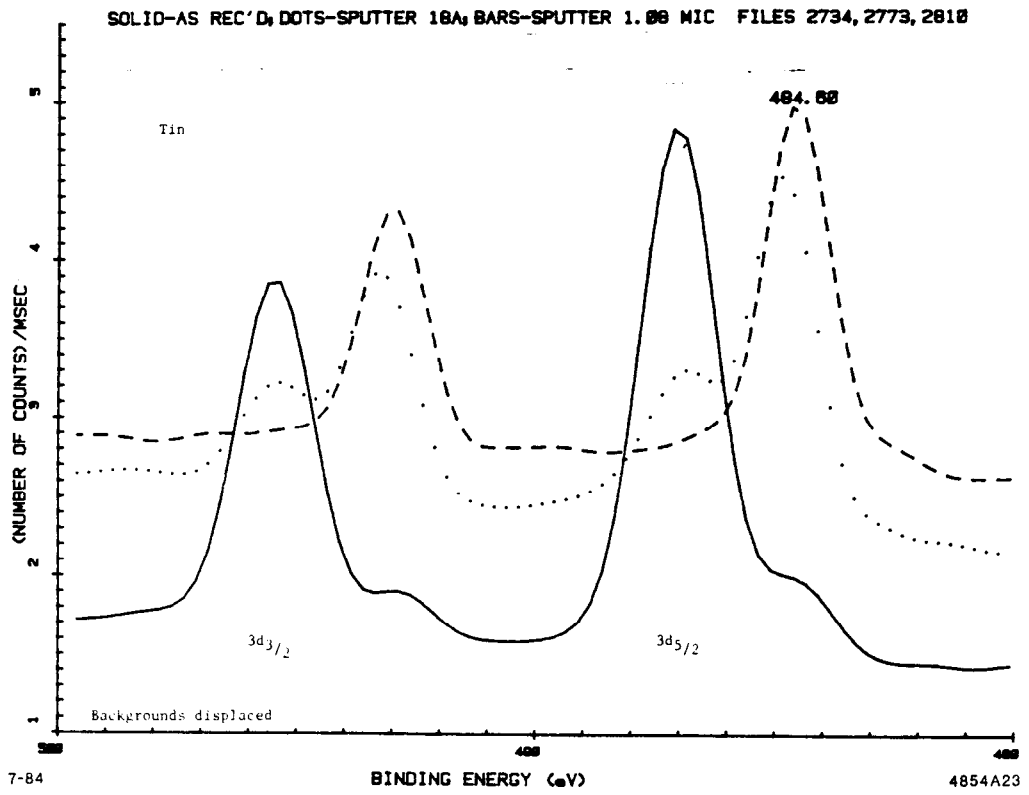


Fig. K5

SIMS

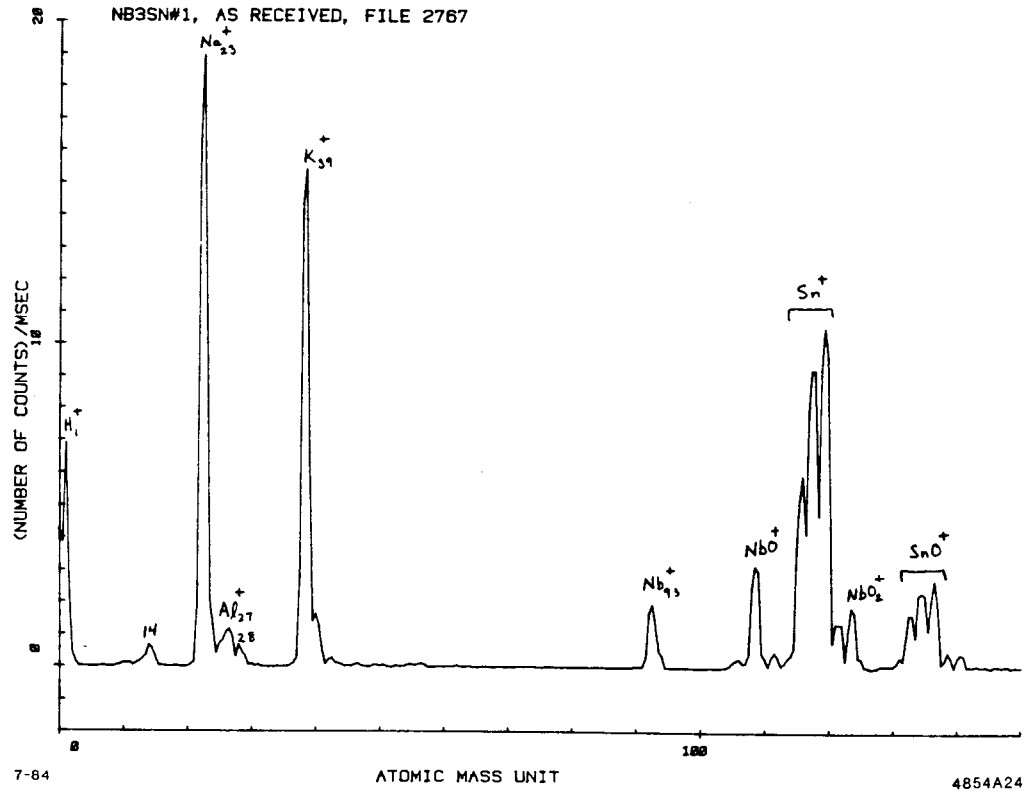


Fig. K6

SIMS

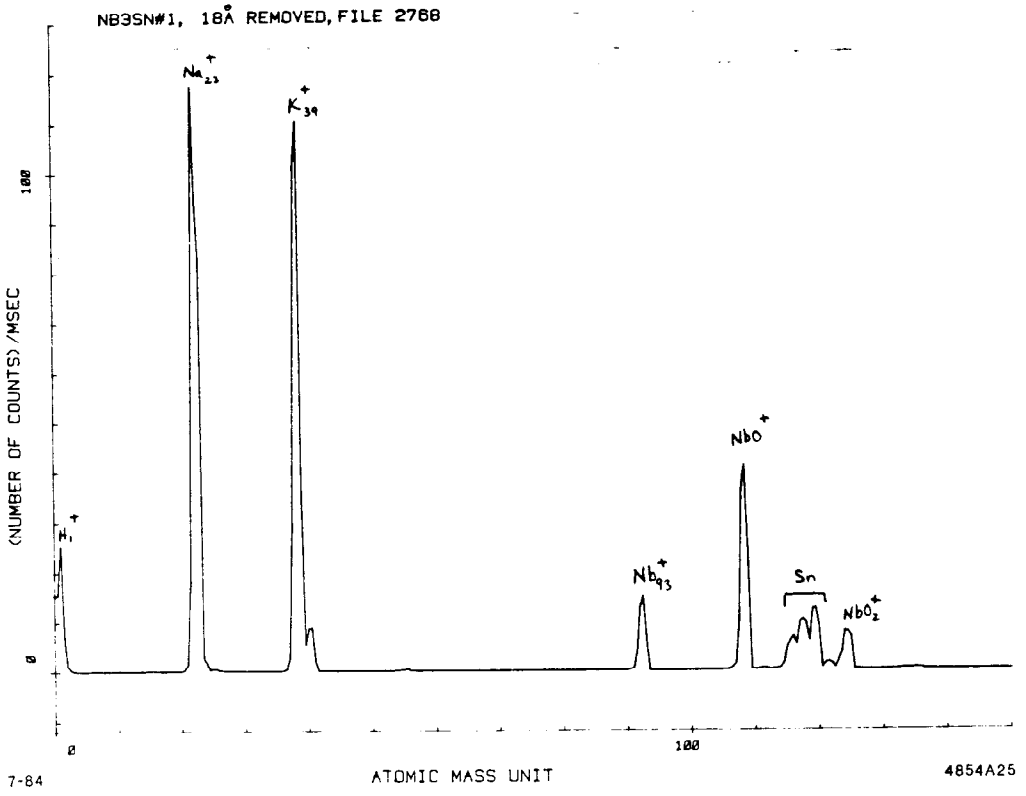


Fig. K7

SIMS

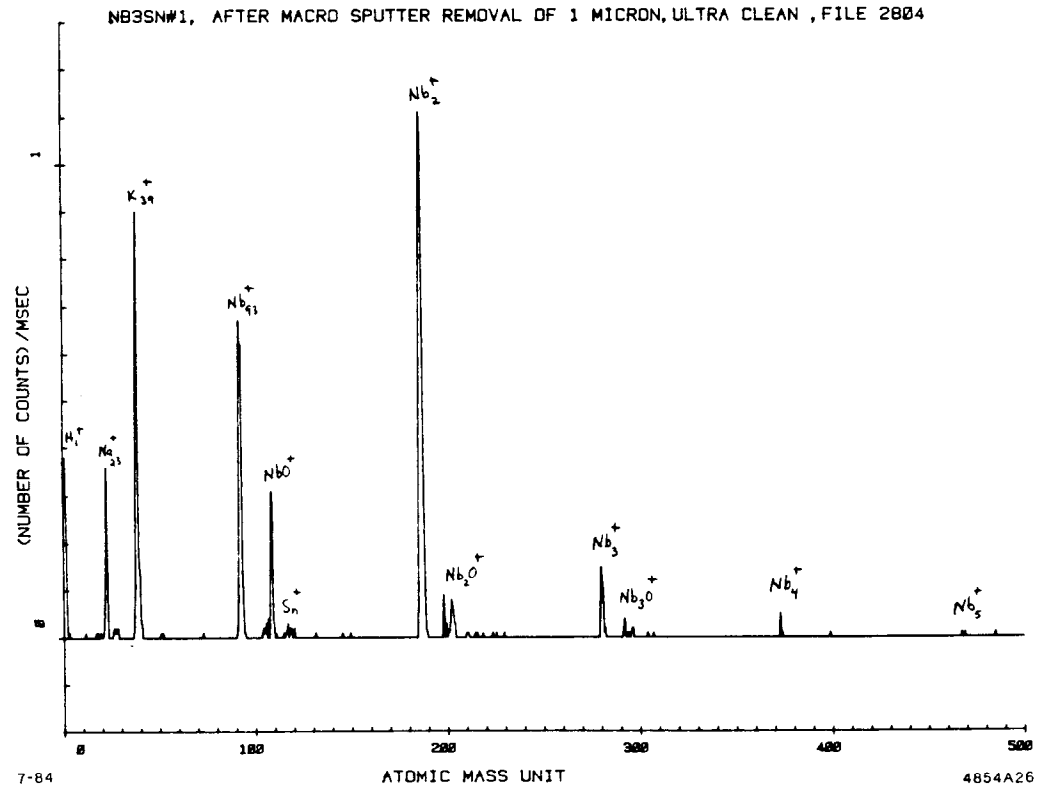


Fig. K8

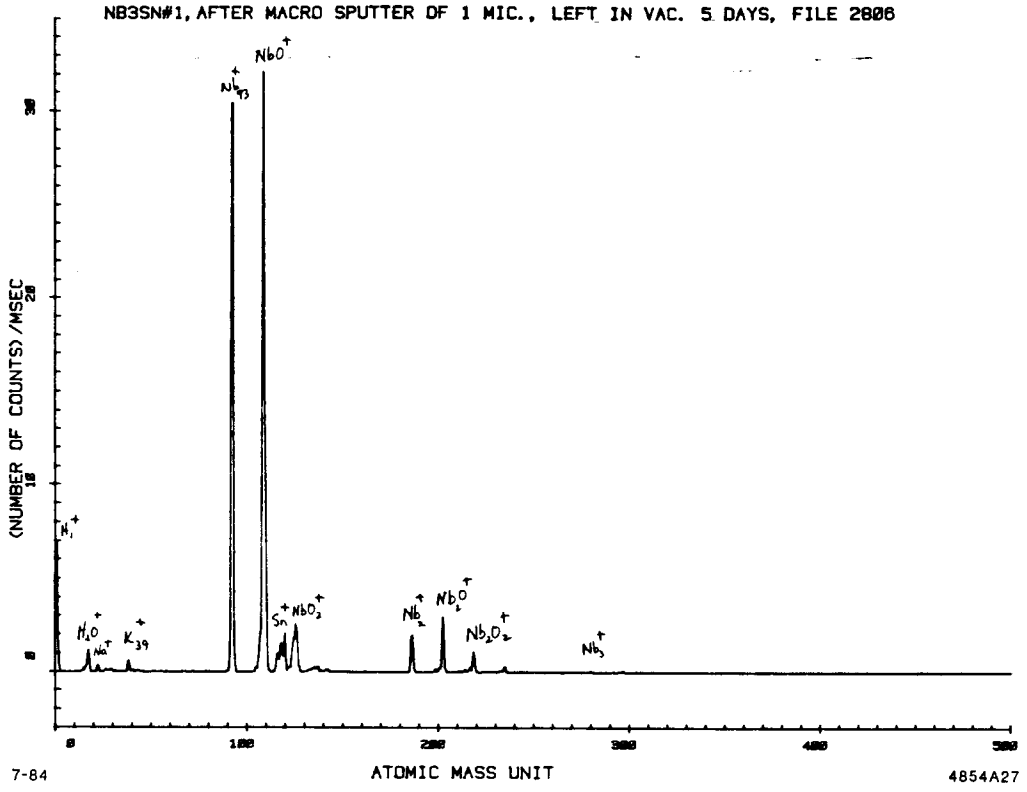


Fig. K9

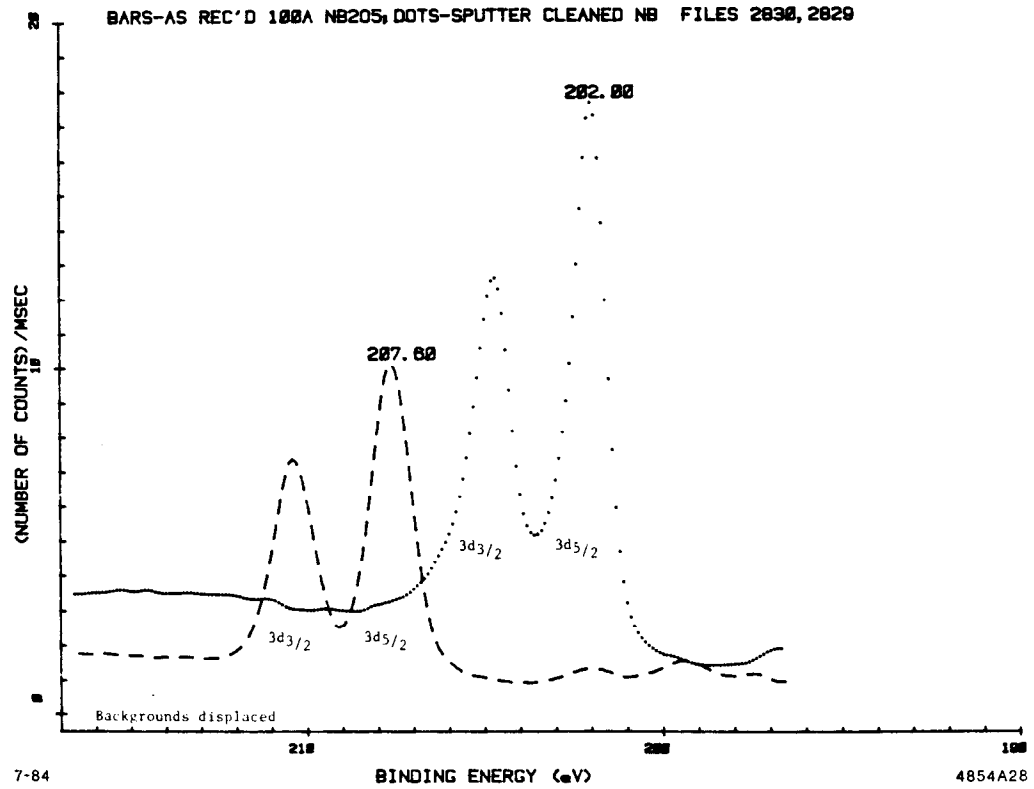


Fig. K10

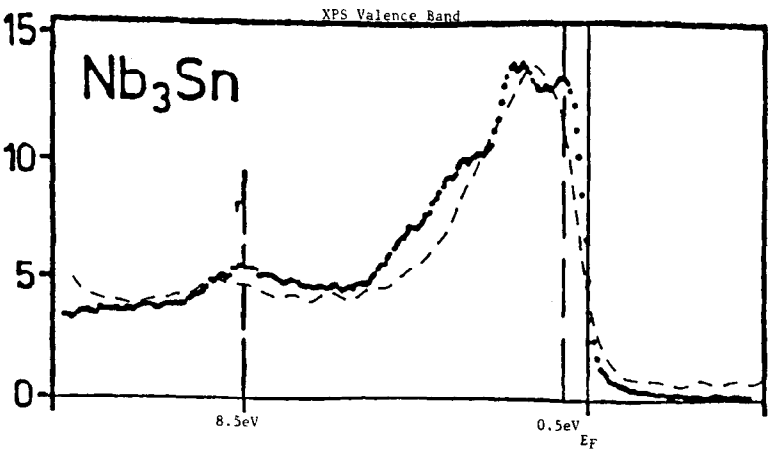


Fig. K11 Dots - from [Höchst (1976)]; Bars - Clean $3\mu Nb_3Sn$